CZECH TECHNICAL UNIVERSITY IN PRAGUE
FACULTY OF NUCLEAR SCIENCES AND PHYSICAL ENGINEERING

HABILITATION LECTURE

QGP Tomography with Jets

Prague, 2021 **RNDr. Jana Bielčíková, Ph.D.**

ČESKÉ VYSOKÉ UČENÍ TECHNICKÉ V PRAZE
FAKULTA JADERNÁ A FYZIKÁLNĚ INŽENÝRSKÁ

HABILITAČNÍ PŘEDNÁŠKA

Tomografie QGP pomocí jetů

Praha, 2021 **RNDr. Jana Bielčíková, Ph.D.**

Tomografie QGP pomocí jetů

Abstrakt

Habilitační přednáška je věnována tomografii horké a husté jaderné hmoty, kvark-gluonového plazmatu, produkovaného ve vysokoenergetických jádro-jaderných srážkách na urychlovači RHIC v laboratoři BNL a urychlovači LHC v laboratoři CERN. Konkrétně je v přednášce kladen důraz na tomografii pomocí jetů, která v poslední dekádě zaznamenala velký pokrok. Jety, kolimované spršky hadronů, vznikají evolucí vysoce virtuálních partonů z tvrdého rozptylu v počáteční fázi srážky. Přímá rekonstrukce jetů na velkém a silně fluktuujícím pozadí ostatních částic vznikajících ve srážce je však náročná. Proto jsou používány i jiné metody, jakými je studium inkluzivních spekter částic s vysokou příčnou hybností nebo di-hadronové korelace. Habilitační přednáška shrnuje nedávné výsledky produkce jetů od energií dosažitelných na urychlovači RHIC po energie na LHC a kde je to možné, jsou data porovnána s teoretickými modely.

Klíčová slova: QCD, jety, kvark-gluonové plazma, zhášení jetů

QGP Tomography with Jets

Abstract

The habilitation lecture is devoted to tomographic studies of hot and dense nuclear matter, quark-gluon plasma, produced in high-energy nucleus-nucleus collisions at RHIC at BNL and the LHC at CERN, respectively. In particular, the focus is given on jet tomography which witnessed in the last decade many advances. Jets, collimated sprays of hadrons, originate from the evolution of highly virtual partons created in a hard scattering. Direct reconstruction of jets on large and fluctuating background of particles created in heavy-ion collisions is however challenging and other methods such as studies of inclusive particle production with large transverse momentum or di-hadron correlations are explored as well. The habilitation lecture summarizes recent results on jet production from RHIC to LHC energies and wherever possible the data are also compared with theoretical models.

Keywords: QCD, jets, quark-gluon plasma, jet quenching

Contents

1 Why to study heavy-ion collisions? 1
1.1 Phase diagram of QCD matter 1
1.2 Basic properties of Quark Gluon Plasma 3

2 Early measurements of jet quenching 8
2.1 Parton propagation in QCD matter 8
2.2 Inclusive hadron transverse momentum spectra 9
2.3 Di-hadron correlations 11
2.4 Leading hadron bias - toward fully reconstructed jets 13

3 Tomographic studies with reconstructed jets 14
3.1 Limitations coming from the underlying soft backgroud 14
3.2 Measurements of dijet asymmetries 15
3.3 Inclusive jet production 18
3.4 Semi-inclusive hadron-jet production 23
3.5 Medium induced jet broadening 25
3.6 Strangeness production in jets 29
3.7 Jet substructure measurements 31

4 Summary and outlook 33

Chapter 1

Why to study heavy-ion collisions?

This habilitation lecture is devoted to studies of strongly interacting matter under extreme conditions of large temperature and energy density using jets as a tomographic tool. This unique type of matter can be created in nucleus-nucleus collisions at high energies achievable at the Large Hadron Collider (LHC) at CERN and Relativistic Heavy Ion Collider (RHIC) at Brookhaven National Laboratory (BNL). At both, the LHC and RHIC, temperature and energy densities in central nucleus-nucleus collisions reach values which are well above the expected threshold for creation of a deconfined state of nuclear matter, the Quark Gluon Plasma (QGP) [1, 2]. The created matter instead of behaving like a gas of free quarks and gluons, as was intially expected, appears to be more like a liquid with extremely low viscosity approaching the conjectured bound for perfect liquid.

Studies of QGP in heavy-ion collisions have a direct connection with cosmology and astrophysics. About one microsecond after the Big Bang, universe was filled with the QGP and was still too hot for ordinary hadrons such as protons and neutrons to be formed. QCD calculations show that the transition from this primordial hot QCD matter to hadronic matter in the first few microseconds after the Big Bang did not proceed via a first order phase transition but it was a continuous crossover [3, 4]. This is consistent with cosmological observations and current understanding of nucleosynthesis in the early universe [5] which do not manifest any inhomogenities over length scales of centimeters or meter. This also means that the continuous crossover from QGP to hadronic matter did not left behind any fluctuations on length scales much longer than femtometer scale. Experimental studies of heavy-ion collisions are therefore the only possibility how to investigate properties of QGP and the related phase diagram of QCD matter.

1.1 Phase diagram of QCD matter

In the left panel of Figure 1.1 the QCD phase diagram is displayed in a plane of the temperature (T) and the baryon chemical potential (μ_B). The diagram contains a schematic layout of the individual QCD matter phases, along with indications of the regions crossed in the early stages of heavy-ion collisions at various beam energies from the highest achievable energies at the LHC and RHIC colliders down to future experiments at FAIR in GSI Darmstadt in Germany. At high energy densities, QCD calculations on a lattice predict a phase

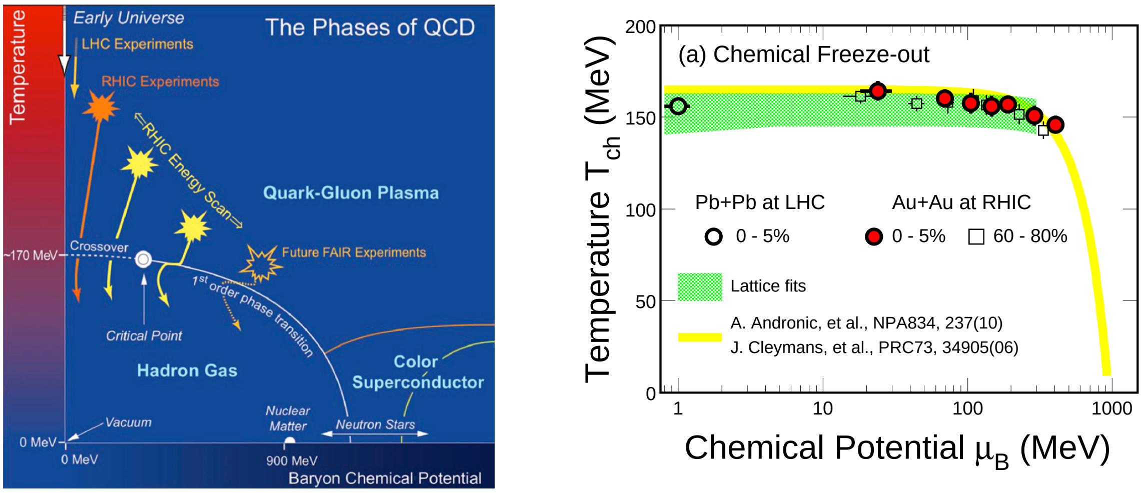

Figure 1.1: Left: A schematic view of the QCD phase diagram [6]. Right: Chemical freeze-out temperature (T_{ch}) as a function of baryonic chemical potential (μ_B) from a statistical model fit to hadron yields in Au+Au collisions at RHIC BES energies [7] and Pb+Pb collisions from the ALICE experiment at the LHC [8, 9]. The yellow band shows the empirical thermal fit results prior to the BES program by a statistical model [10, 11]. The green band represents the lattice QCD results for the region of the cross-over transition [12, 13]. Figure taken from [14].

transition from a hadron gas to the QGP state [1, 2]. This transition should be a crossover at the temperature around 154 MeV for $\mu_B = 0$ (see e.g. [12, 13]). A first-order phase transition and the existence of a critical point at high μ_B is expected in QCD based models (see e.g. [15, 16]) and is currently being searched for at RHIC. RHIC is uniquely positioned to perform such studies due to its flexibility to vary the collision energy which enables to access different regions of the QCD phase diagram. Yields of light flavour hadrons measured in the first phase of the RHIC Beam Energy Scan (BES) program were used to estimate the values of T and μ_B at chemical freeze-out, the point in time when elastic collisions between particles cease as shown in the right panel of Figure 1.1 along with the empirical T_{ch} vs μ_B (yellow band) based on data obtained prior to the BES-I program at RHIC using statistical models [10, 11]. The figure demonstrates the flexibility of RHIC to cover the μ_B region from 20 to 420 MeV, which is absolutely unique among collider facilities. The QCD critical point from the lattice QCD calculations is estimated to be located around $\mu_B \approx 300$ MeV [17, 18], in reach of the BES program at RHIC and a detailed study of the energy range from 7.7 to 19.6 GeV to identify the critical point and the first-order phase transition boundary of the QCD matter phase diagram is currently being pursued in the second phase of the BES data taking to be completed in 2021. We kindly refer the interested reader to e.g. [6, 14] and references therein for further details on results from the BES physics program.

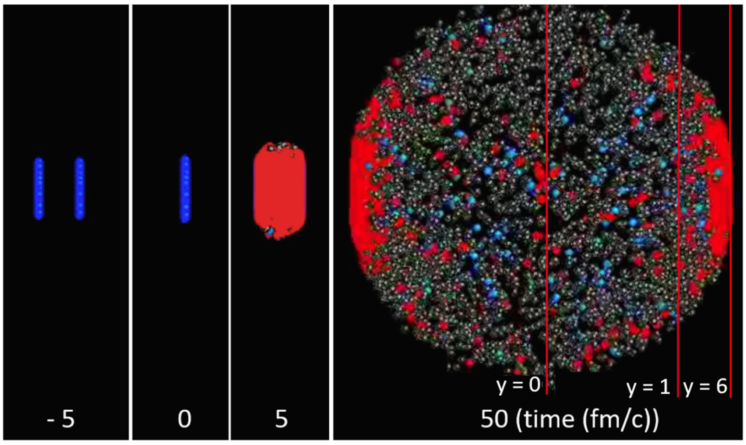

Figure 1.2: Snapshots of a central 2.76 TeV Pb+Pb collision at the LHC at different times with hadrons (blue and grey spheres) as well as QGP (red). The red lines indicate the approximate longitudinal location of particles with rapidity y = 0, 1, and 6, respectively. Figure adapted from [19].

1.2 Basic properties of Quark Gluon Plasma

The QGP matter created in ultrarelativistic heavy-ion collisions has remarkable properties. The maximum energy density occurs just as the two highly Lorentz contracted nuclei collide followed by a fast expansion of the collision zone and subsequent cooling as depicted on the cartoon in Figure 1.2. The entropy, which is produced in these collisions as well as energy density are enormous. At the LHC energy of 5 TeV the final state contains as many as 30,000 particles and about 1,500 particles are produced at the top RHIC energy of 0.2 TeV. A rough estimate of the energy density based on the Bjorken formula [20] and the total transverse energy of particles produced at midrapidity in the most central (0-5%) Pb+Pb collisions leads to about 16 GeV/fm^3 at the LHC and 5.4 GeV/fm^3 [21] in central Au+Au collisions at RHIC, respectively. The increase of the energy density by a factor of three between RHIC and LHC corresponds to about 30% increase in the temperature of the QGP produced at the LHC compared with RHIC. The average energy density achievable at the LHC is about 30 times larger than that inside a typical hadron 0.5 GeV/fm^3. The QCD calculations on lattice [22] showed that matter in thermal equilibrium at a temperature of 300 MeV has an energy density of $\approx 12T^4 = 12.7$ GeV/fm^3. This indicates that the quarks and gluons produced in the collision cannot be described as a collection of individual hadrons.

On the other hand they are also far from being independent. The quarks and gluons are strongly coupled to each other and give rise to a collective medium that expands and flows [23, 24]. In case of non-central collisions, the overlap region of the two colliding Lorentz contracted nuclei has a characteristic lenticular shape in the transverse plane. This deviation from circular symmetry along with the lumpiness and fluctuations of the colliding nuclei give rise to anisotropies in the pressure of the hydrodynamically expanding fluid. These in turn translate to anisotropies in the expansion velocity and azimuthal momentum distribution of particles. Study of azimuthal anisotropies of particles produced, commonly referred to as 'anisotropic collective flow' [25], are sensitive to the properties of Equation of State (EOS) of the nuclear

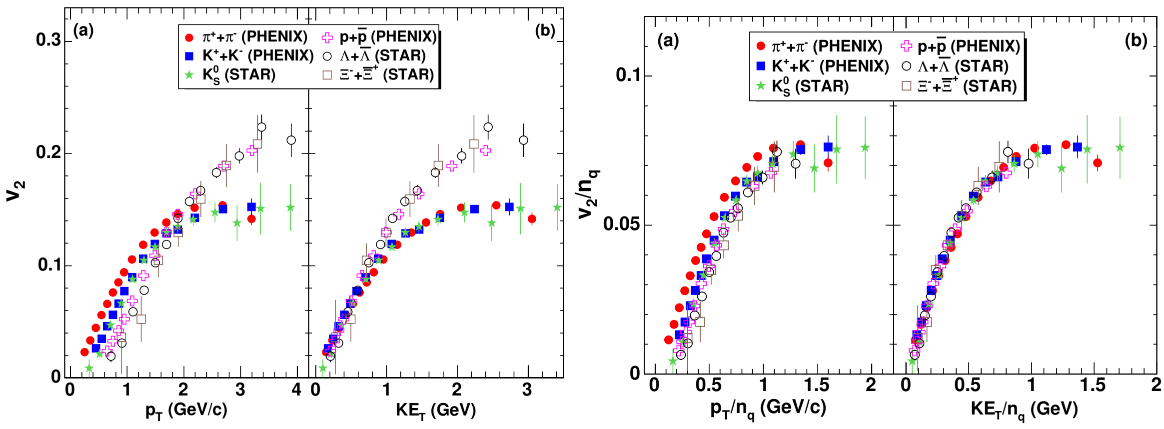

Figure 1.3: (Left) Light-flavour hadron v_2 vs p_T and KE_T in minimum bias Au+Au collisions at $\sqrt{s_{NN}}$ = 200 GeV. (Right) Same as on the left, but the v_2 values are scaled by the number of constituent quarks n_q. The STAR data are from [28, 29]. Figures are taken from [30].

matter. These anisotropies are commonly characterized by a Fourier decomposition of the azimuthal particle distribution with respect to the reaction plane angle ($\psi_{\rm RP}$) [26, 27] defined by the beam direction and impact parameter between the centers of two colliding nuclei:

$$\frac{\mathrm{d}N}{\mathrm{d}\varphi} \propto 1 + 2\sum_{n=1}^{\infty} v_n \cos(n(\varphi - \psi_{\rm RP})), \tag{1.1}$$

where the flow coefficient v_n is the magnitude of the n-th order anisotropic flow. The first two Fourier coefficients v_1 and v_2 are called directed and elliptic flow, respectively, but higher Fourier harmonics are also being explored in last years. The third-order Fourier coefficient v_3 (triangular flow), is generated by fluctuations in the initial distribution of nucleons and gluons in the overlap region of the two colliding nuclei. The fourth-order Fourier coefficient v_4 (quadrangular flow) originates from both initial geometry of the colliding nuclei and initial state fluctuations but is also sensitive to the non-linear hydrodynamic response of the QCD medium.

Here I would like to focus on v_2 studies and their connection with the QCD matter properties. The link is provided by hydrodynamics which connects the QCD matter EOS, transport coefficients and the flow properties imprinted in the measured hadron spectra and hadron azimuthal anisotropies. In the hydrodynamical models, elliptic flow results from pressure gradients due to the initial spatial asymmetry (eccentricity) of the collision zone in non-central heavy-ion collisions. At low transverse momentum ($p_{\rm T} < 2$ GeV/c), a mass ordering of v_2 values is observed for the light-flavour hadrons measured in Au+Au collisions at the top RHIC energy $\sqrt{s_{NN}}$ = 200 GeV by the STAR and PHENIX experiments [28–30] as demonstrated in the left panel of Figure 1.3. If driven by hydrodynamic pressure gradients, the v_2 values for each particle type should scale with their respective transverse kinetic energy $KE_T = m_T - m$, where m (m_T) is the particle (transverse) mass. The validity of this scaling is demonstrated in the right panel of Figure 1.3. When quantitatively compared with hydrodynamical calculations the magnitude of the differential v_2 in the low-$p_{\rm T}$ range is found to be in a good agreement with hydrodynamical calculations for ideal fluid with a shear

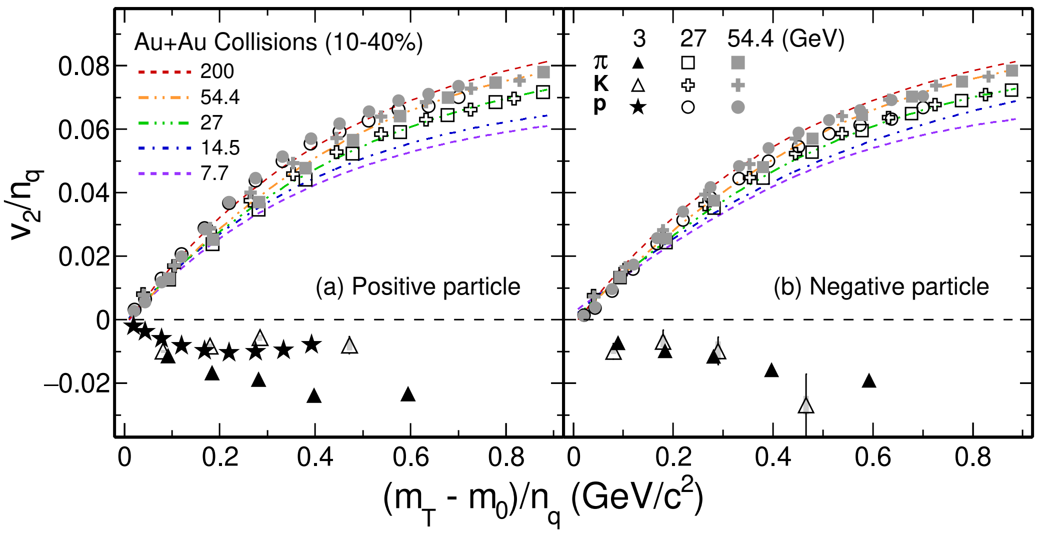

Figure 1.4: Elliptic flow v_2 scaled by the number of constituent quarks as a function of scaled transverse kinetic energy for pions, kaons and protons from Au+Au collisions in 10-40% centrality at $\sqrt{s_{NN}}$ = 3, 27, and 54.4 GeV. Colored dashed lines represent the scaling fit to data in 7.7, 14.5, 27, 54.4, and 200 GeV Au+Au collisions. Figure adapted from [32].

viscosity to entropy density ratio (η/s) that approaches the conjectured theoretical lower limit from the anti-de Sitter/conformal field theory (AdS/CFT) correspondence of $1/4\pi$ [31]. The data from RHIC provided for the first time an evidence for the production of a strongly interacting QGP whose evolution is similar to that of a "perfect" fluid and can be described by ideal hydrodynamics. It is clear that the range of applicability of ideal hydrodynamics is affected by the onset of dissipative effects as well as degree of thermalization of the system created in heavy-ion collisions at high energies.

For higher p_{T} values the mass ordering is broken and a distinct baryon-meson splitting of v_2 is observed as manifested in the left panel Figure 1.3. This splitting is indicative of v_2 being dependent on the constituent quark composition of a given particle as demonstrated in the right panel of the figure, where the measured v_2 and KE_T values are scaled by the respective number of constituent quarks (n_q) ($n_q = 2$ for mesons and $n_q = 3$ for baryons). This constituent quark scaling of v_2 has been attributed to the dominance of the quark coalescence hadronization mechanism from a thermalized state of flowing partonic matter [33–35]. Subsequent studies [36] confirmed the NCQ scaling to hold to $KE_T/n_q = 1.5$ GeV in central Au+Au collisions at the top RHIC energy. However, significant deviations from the NCQ scaling were found in non-central Au+Au collisions, starting already from the 10–20% centrality class. This observation indicates that parton fragmentation and the associated energy loss may play an important role in generating the observed azimuthal anisotropy of emitted particles. At LHC energies, the validity of the NCQ scaling has been scrutinized as well [37–39]. In the region, where the quark coalescence is expected to be the dominant process, a deviation of ± 20% (15%) from the NCQ scaling is found for the most central (peripheral) Pb+Pb collisions. Recently released STAR data from the BES program at RHIC

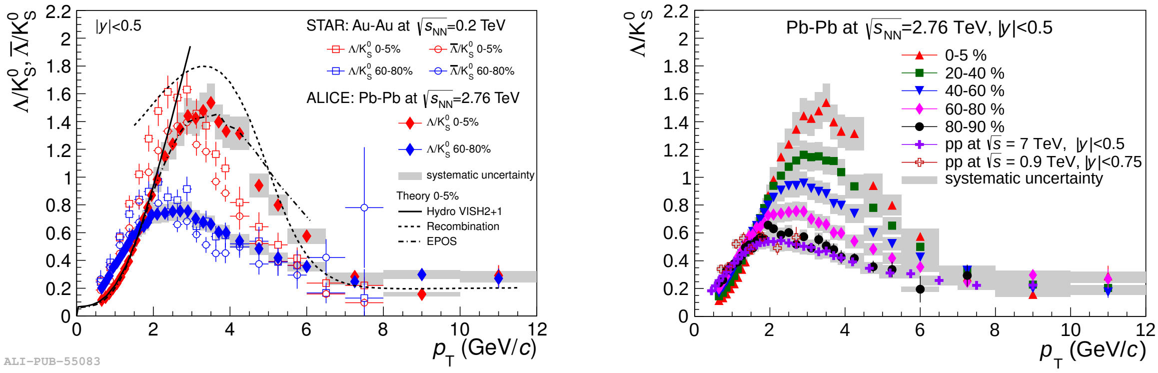

Figure 1.5: (Left) Λ/K^0_S ratio as a function of p_T for central and peripheral Au+Au collisions at $\sqrt{s_\mathrm{NN}} = 0.2$ TeV measured by STAR [40] and Pb+Pb collisions at $\sqrt{s_\mathrm{NN}} = 2.76$ TeV measured by ALICE. The lines show the corresponding ratios from a hydrodynamical model [41–43], a recombination model [44] and the EPOS model [45], respectively. (Right) The Λ/K^0_S ratio for multiple centrality classes in Pb+Pb collisions at $\sqrt{s_\mathrm{NN}} = 2.76$ TeV measured by ALICE and compared with p+p collisions at $\sqrt{s} = 0.9$ and 7 TeV. The figure is adapted from [46].

demonstrate that the partonic collectivity clearly disappears for very low collision energies around $\sqrt{s_{NN}} = 3$ GeV [32] as demonstrated in Figure 1.4.

Formation of hadrons by colour confinement of quarks and gluons is a complex, non-perturbative QCD process. As of today, there is no rigorous theoretical description of hadronization and it must be modelled phenomenologically. Experimental measurements of identified particle production presented in case of anisotropic flow measurements constitute also essential input to better understand hadronization mechanisms. A fragmentation hadronization scheme, which has been tested and accepted for high-momentum transfer processes, encounters problems when trying to explain the enhancement in baryon-to-meson ratios for light hadrons in the transverse momentum (p_T) region of $2 < p_T < 6\,\mathrm{GeV}/c$ in heavy-ion collisions at RHIC [47,48]. The existence of this baryon-to-meson enhancement was later also confirmed by measurements at the LHC [46]. In Figure 1.5 we demonstrate this observation on the measurement of strange baryon-to-meson ratio Λ/K^0_S by the STAR and ALICE experiments. Essentially independently of the collision energy, the observed Λ/K^0_S ratio is similar and is significantly enhanced in central heavy-ion collisions with a pronounced peak around $p_\mathrm{T} \simeq 3$ GeV/c. Recent experimental data at RHIC [49] provide a clear evidence that the baryon-to-meson enhancement is also present for heavier, charm quarks in central Au+Au collisions at $\sqrt{s_{NN}} = 200$ GeV. There is also a first measurement from ALICE at the LHC in minimum bias Pb+Pb collisions at $\sqrt{s_{NN}} = 5.02$ TeV [50] for $6 < p_T < 12\,\mathrm{GeV}/c$, but no data at the LHC energy exist yet for the lower p_T range where the baryon-to-meson enhancement is expected to be most pronounced.

The most common hadronization mechanism which could play a role in presence of QGP is a coalescence/recombination hadronization mechanism. In this mechanism, hadrons can be formed via recombination of partons that are close by in a densely populated phase space. Contrary to the parton fragmentation, recombination leads to production of hadrons with momenta larger than those of their parent partons. This fact in combination with the steeply falling p_{T} distribution of quarks favors parton recombination over fragmentation in hadronization in a certain p_{T} region. Consequently, at a given particle p_{T} in this region of dominance production of a baryon composed of three valence quarks is more probable than production of a meson at the same p_{T} which has to be formed from a pair of a quark and anti-quark. This simple mechanism would thus naturally lead to an enhanced ratio of baryon to meson yields and has been implemented in several phenomenological models, see e.g. [34, 35, 51–54].

Chapter 2

Early measurements of jet quenching

In order to capture elusive characteristics of the QGP, which once created lives only for a very short time, multiple observables have to be explored. Heavy quarks, quarkonia and jets, commonly referred to as hard probes, originate from the hard parton interactions in the first moments of the collision. These partons then evolve, decay, and radiate while traversing the medium experiencing thus the whole time evolution of the medium. Therefore hard probes are considered as an ideal tomographic probes of the QCD matter properties. Hard probes are however rare as most of the parton interactions shortly after the collision of highly Lorentz contracted nuclei are soft, i.e they involve only small transverse momentum transfer.

In this lecture the focus is on jets, collimated sprays of hadrons that originate from hard parton scattering. In elementary particle collisions, such as proton-antiproton collisions explored in past at the Tevatron in Fermilab or proton-proton collisions currently investigated at the CERN LHC, jets are commonly studied via their direct reconstruction using various jet finding algorithms. In heavy-ion collisons, large and fluctuating background in combination with small jet cross sections makes direct jet reconstruction challenging and alternative methods are used as well as we will describe below.

2.1 Parton propagation in QCD matter

In QCD, the quark and gluon stopping in matter are known to exhibit the same qualitative behaviour as in QED. The energy loss of an energetic quark or gluon, commonly referred to as partons, penetrating QCD medium is a fundamental probe of dynamical properties of the medium. Partons propagating through the medium loose their energy in two ways: parton collisions with constituents of the medium referred to as collisional (elastic) energy loss and by radiative (inelastic) energy loss via gluon bremsstrahlung. While at low momentum, the dominant energy loss process is the collisional energy loss, at high momentum parton energy loss is primarily connected with inelastic radiative processes in which the scattering centers trigger a gluon emission. Already the first studies of medium induced gluon bremsstrahlung [55–62] realized that radiative parton energy loss is the dominant mechanism in large QCD media. These early calculations were followed by many others using different approaches

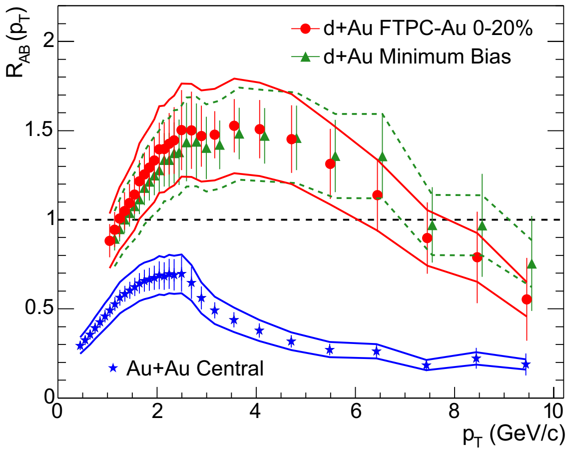

Figure 2.1: Nuclear modification factor R_{AA} for inclusive charged-particle production in d+Au and Au+Au collisions at $\sqrt{s_{NN}} = 200$ GeV measured by the STAR experiment. The bands represent the normalization uncertainties, which are highly correlated point-to-point and between the two d+Au distributions. Au+Au data points are from [67]. Figure is taken from [68].

and improvements, see e.g. the review articles [63–66] and original references therein. The different approximations used to describe the medium (e.g. BDMPS-Z, GLV, Higher-Twist) naturally lead to different ways to specify the medium properties. It has become conventional to translate the primary model parameters into an effective parameter $\hat{q}$ that has the physical interpretation of an averaged squared momentum transfer between the medium and the fast parton per unit path length λ traversed

$$\hat{q} = \langle q_{\perp}^2/\lambda \rangle. \tag{2.1}$$

2.2 Inclusive hadron transverse momentum spectra

Jet interaction with QCD matter and the related jet quenching effect was first observed as the suppression of inclusive charged hadron production at large p_{T} in central Au+Au collisions at the top RHIC energy relative to p+p collisions. In order to quantify the amount of the suppression, the nuclear modification factor R_{AA} is introduced and defined as the ratio of the particle p_{T} spectra in a given centrality bin in A+A collisions relative to p+p collisions scaled by the respective number of binary nucleon-nucleon collisions [67, 69–71]:

$$R_{\mathrm{AA}} = \frac{dN^{\mathrm{AA}}/dp_T}{\langle N_{\mathrm{coll}} \rangle dN^{pp}/dp_T} = \frac{dN^{\mathrm{AA}}/dp_T}{T_{\mathrm{AA}}\, d\sigma^{pp}/dp_T}, \tag{2.2}$$

where N^{AA} and N^{pp} are the charged-particle yields in A+A and p+p collisions, respectively, and σ^{pp} is the charged-particle cross section in p+p collisions. The ratio of $\langle N_{\mathrm{coll}} \rangle$ with the total inelastic p+p cross section, defined as $T_{\mathrm{AA}} = \langle N_{\mathrm{coll}} \rangle / \sigma^{pp}_{\mathrm{inel}}$, is the nuclear overlap function that can be calculated from a Glauber model of the nuclear collision geometry [72].

One of these early R_{AA} measurements at RHIC is shown in Figure 2.1 and demonstrates that at high p_{T}, the R_{AA} reaches only a value of around 0.2. This observation in other words

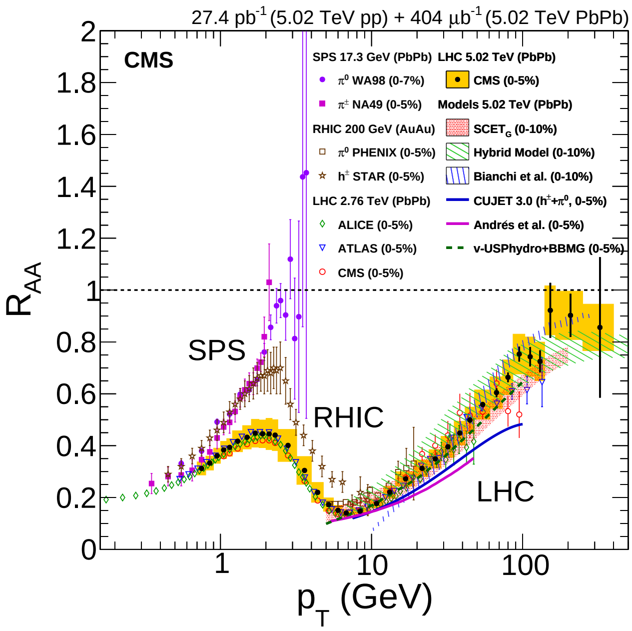

Figure 2.2: Collection of measurements of nuclear modification factors in central heavy-ion collisions at four different center-of-mass energies: for neutral pions (SPS, RHIC) and charged hadrons (SPS, RHIC, LHC). The LHC data in Pb+Pb collisions at $\sqrt{s_{NN}}$ = 5.02 TeV are compared to model predictions [73–77]. Figure is taken from [78].

means that the charged particle production is suppressed by a factor of five in central Au+Au relative to p+p collisions at the top RHIC energy. The fact that this is not due to initial state effects on particle production was confirmed by the measurement in d+Au collisions, a small collision system, where no QGP or dense nuclear matter is expected to be formed. The R_{AA} in d+Au collisions as can be seen from Figure 2.1 is reaching values slightly above one which was attributed to nuclear shadowing and its centrality dependence [79, 80]. Measurements with larger statistics, e.g. by the PHENIX experiment at RHIC [81] demonstrated that although the suppression slowly decreases with increasing p_{T} it still persists even at p_{T} = 20 GeV/c.

At an order of magnitude higher collision energy of $\sqrt{s_{NN}}$ = 2.76 and 5.02 TeV accessible at the LHC at CERN, the ALICE, ATLAS and CMS measurements of charged-particle R_{AA} also revealed a large suppression of charged-particle production relative to small collision systems (p+p and p+Pb) [78, 82–84] suggesting again that the large suppression observed in Pb+Pb collisions is a hot medium effect. Quantitatively, the charged-particle production was found to be suppressed by a factor of about seven for p_{T} = 5–10 GeV/c and the observed suppression decreases with increasing p_{T} to approach roughly a value of about 2 at p_{T} = 40–100 GeV/c reachable with the Run1 LHC statistics. In Figure 2.2 the RHIC and the Run1 LHC R_{AA} measurements are presented together with most recent charged-particle R_{AA} results for Pb+Pb collisions at the LHC energy frontier of $\sqrt{s_{NN}}$ = 5.02 TeV (Run2), where the luminosities allowed to measure the R_{AA} out to amazing p_{T} = 400 GeV/c. At these very high transverse momenta the R_{AA} reaches a value of about 0.9 and within uncertainties is compatible with no suppression. Comparing the RHIC and LHC results, it is interesting to note that the R_{AA} values have at all collision energies a rising trend at low transverse

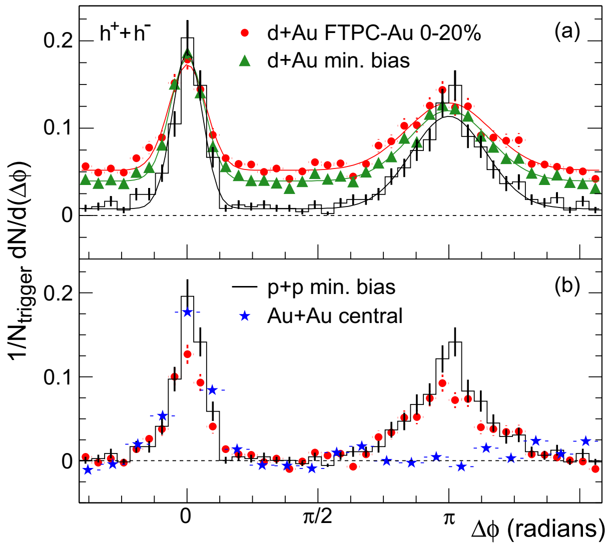

Figure 2.3: (Top) Two-particle azimuthal distributions for minimum bias and central d+Au and p+p collisions at $\sqrt{s_{NN}} = 200$ GeV. (Bottom) Comparison of two-particle azimuthal distributions for central d+Au collisions to p+p and central Au+Au collisions [85]. Trigger particles were selected within $4 < p_T^{\text{trigger}} < 6$ GeV/c and associated particles with 2 GeV/$c < p_T^{\text{associated}} < p_T^{\text{trigger}}$. Figure is taken from [68].

momenta up to about $p_{\mathrm{T}} = 2$ GeV/c followed by local minima at RHIC and the LHC located around $p_{\mathrm{T}} = 6$–7 GeV/c. At higher p_{T}, the observed suppression at RHIC and LHC is within uncertainties the same. With increasing collision energy, the charged-particle spectra flatten at high p_{T} and if the average energy loss at given p_{T} is fixed, the flattening of the spectra would cause the nuclear modification factor to exhibit less suppression. The similar values of R_{AA} at RHIC and the LHC thus indicate that the effect of particle spectra flattening could be balanced by a larger average energy loss at LHC energies. Comparison of the charged-particle R_{AA} with available state-of-the art model calculations displayed in Figure 2.2, shows that the models are generally able to reproduce the measured data, although differences can be found among them after a closer inspection.

2.3 Di-hadron correlations

These experimental findings on 'jet quenching' via inclusive hadron p_{T} spectra were shortly after corroborated by studies of di-hadron correlations relative to a particle with large p_{T} [68, 85–87], commonly referred to as a trigger particle, which is expected to approximate the direction of the jet axis. Di-hadron correlations involve measurement of distributions of relative azimuthal (φ) and pseudo-rapidity (η) differences of particles with lower p_{T} (called associated particles) relative to the trigger particle. In di-hadron correlations, jets would manifest themselves as one peak centered around ($\Delta\varphi = 0$, $\Delta\eta = 0$) relative to the trigger particle and referred therefore to as a near-side peak and another (away-side) peak at $\Delta\phi \approx \pi$ and elongated in pseudorapidity corresponding to the recoil jet. It is important to keep in mind that at low p_{T}, resonance decays as well as femtoscopic correlations also contribute to

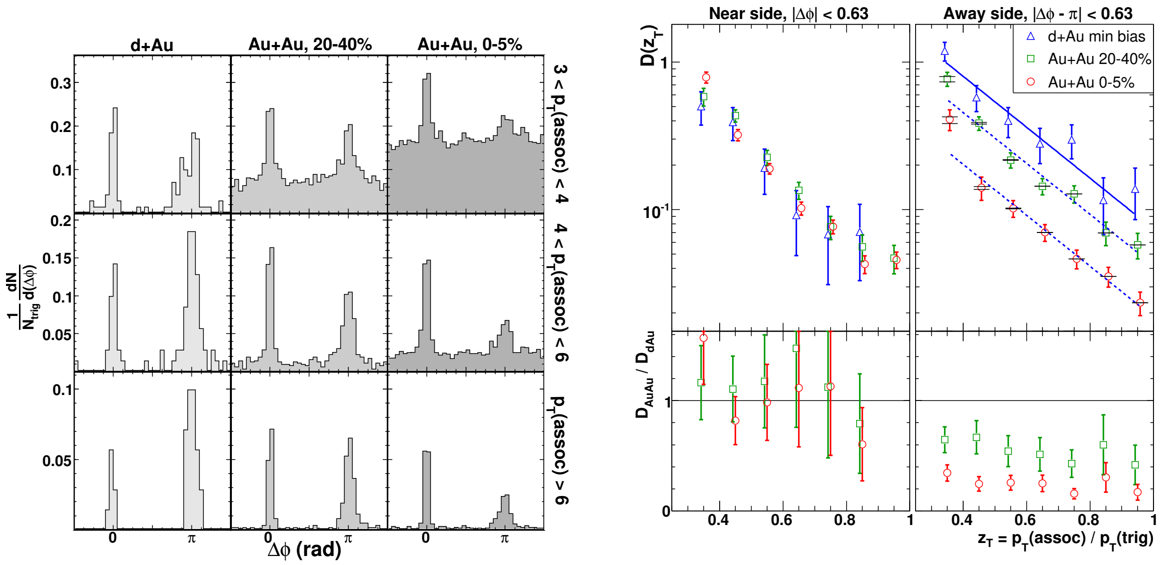

Figure 2.4: (Left) Azimuthal correlations of high-p_T charged hadrons with $8 < p_T^{\rm trigger} < 15$ GeV/c in d+Au and Au+Au collisions at $\sqrt{s_{NN}} = 200$ GeV. (Right) Trigger-normalized charged hadron fragmentation function $D(z_T)$ for near- and away-side correlations in the same collision system. Horizontal bars on away-side show systematic uncertainty due to background subtraction. Lower panels display the ratio of $D(z_T)$ for Au+Au relative to d+Au collisions. Figures adapted from [86].

the near-side correlation peak and all these genuine correlations sit on top of an anisotropic flow modulated background which has to be subtracted. In these measurements the jet quenching effect manifested itself by a disappearance of the away-side jet at intermediate $p_{\rm T}$ = 2–6 GeV/c compensated by increased production of low-$p_{\rm T}$ particles. The by now iconic figure of the disapperance of the away-side correlation peak at intermediate $p_{\rm T}$ is displayed in Figure 2.3.

Increasing the $p_{\rm T}$ of the trigger particle, a narrow back-to-back peak emerges above the background for all Au+Au collision centralities studied as displayed in Figure 2.4 [86]. The per-trigger normalized yield of away-side correlation peak is found to be strongly suppressed. In fact, the level of suppression reaches that of inclusive charged-hadron production, supporting thus the picture of creation of a very opaque medium in Au+Au collisions at RHIC. Interestingly, the width of the away-side correlation peak corresponding to the punch-throuch jets shows no dependence on collision system or centrality. The medium effects on dijet fragmentation were explored in more detail using the transverse momentum distributions of associated charged hadrons by extracting the per-trigger normalized fragmentation function $D(z_T)$, where $z_T = p_T^{\rm associated}/p_T^{\rm trigger}$, which is displayed in the right panel of Figure 2.4. The near-side fragmentation is found to be independent of collision system and centrality which could be due to a geometrical bias toward shorter in-medium path lengths (referred to as the *surface bias*) as discussed e.g. in [88–91]. Moreover, energy-independent energy loss which would generate a partonic energy distribution suppressed in Au+Au but similar in shape to that in p+p collisions, with the lost energy carried away by low-$p_{\rm T}$ hadrons, could lead to similar observation.

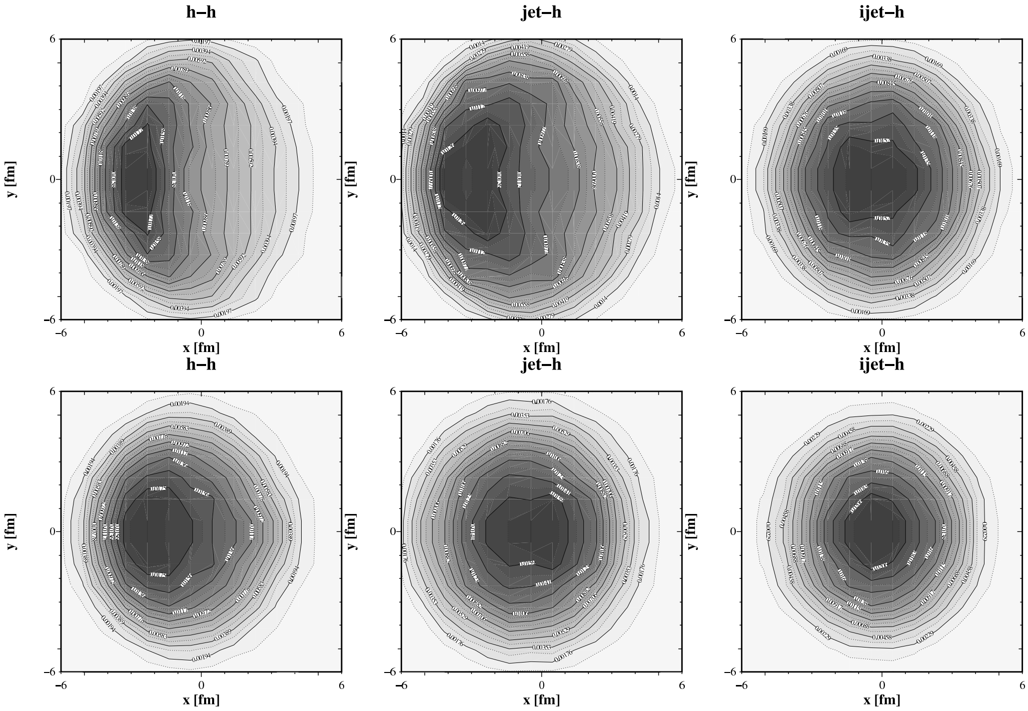

Figure 2.5: Conditional distribution of production vertices in the transverse plane, given a trigger with observed energy E_{obs} between 12 and 15 GeV in 0-10% central $\sqrt{s_{NN}} = 200$ GeV Au+Au collisions (top row) and 0-10% central $\sqrt{s_{NN}} = 2.76$ TeV Pb+Pb collisions (bottom row) for hadron triggers (left), a jet definition used by STAR (middle) and an idealized jet definition (right). In all cases, the trigger object momentum vector defines the $-x$ direction. Figures taken from [92].

2.4 Leading hadron bias - toward fully reconstructed jets

Measurements with leading hadrons are, however, known to suffer from several limitations. The leading hadrons are a mixture of parent quarks and gluons and as their fragmentation product carry only a part of parton's original energy. In addition, di-hadron measurements are influenced by a surface bias as leading hadrons predominantly originate from the surface of the asymmetric collision zone. It is however important to keep in mind that when going from the top RHIC energy of 200 GeV to the LHC energy of 2.76 TeV and keeping the trigger particle momentum fixed, the resulting bias is different as detailed in [92] and demonstrated in Figure 2.5. At the higher collision energy, the hard collision probes the nuclear initial state at lower x and consequently more gluon-dominated regime. The parton momentum spectrum gets harder with increasing collision energy, which implies weakening of the kinematic bias and consequently also weakening of the correlation between parton momentum and leading hadron or jet momentum in general. One should not however forget that at larger collision energy, there is more bulk matter produced which strenghtens the geometrical bias. As the kinematic range available inreases with $\sqrt{s}$, and the medium density as a weak power of $\sqrt{s}$, an overall weakening of the geometrical bias is expected.

Chapter 3

Tomographic studies with reconstructed jets

Although studies of nuclear modification factors of inclusive particle production and di-hadron correlations bring useful insights to jet quenching and are also studied at the LHC energies as we discussed in the previous chapter, the ultimate goal is to use fully reconstructed jets. First pioneering measurements with reconstructed jets were conducted by the STAR experiment at RHIC more than ten years ago [93, 94] but detailed investigation of reconstructed jets started at the LHC energies in Pb+Pb collisions about ten years ago. The jet studies currently include a large variety of observables explored: inclusive jet spectra and related jet R_{AA}, hadron-jet and jet-hadron correlations, or dijet asymmetries but also observables related to jet shapes and jet substructure. Here we review some of the most important studies performed.

3.1 Limitations coming from the underlying soft backgroud

Before entering the discussion of various jet observables, let us take a moment and discuss which limitations of jet reconstruction brings underlying background of soft particles created in a typical high-energy heavy-ion collision. At the LHC energy the average charged particle transverse momentum density for particles with $p_{\mathrm{T}} > 0.15$ GeV/c increases steeply with collision centrality as shown in Figure 3.1 and the average background density reaches about 140 ± 18.5 GeV/c per unit area in central Pb+Pb collisions. At the top RHIC energy, the corresponding value of the average background density and its standard deviation per unit area for $p_{\mathrm{T}} > 0.2$ GeV/c corresponds to 31 ± 3 GeV/c in central Au+Au collisions [95]. To bias the jet reconstruction as least as possible, it is advisable to reconstruct jets using a low transverse momentum threshold applied on their constituents. However, this at the same time means that the influence of the background will be the largest. In ALICE the threshold on p_{T} of jet constituents is typically set to $p_{\mathrm{T}} > 0.15$ GeV/c and in STAR it corresponds to 0.2 GeV/c. This choice of the p_{T} constituent threshold is different to that in typical heavy-ion jet analyses carried out by the ATLAS and CMS experiments at the LHC, where jet constituents are often accepted if they have a minimal p_{T} of the order of GeV/c. Although the approach adopted by ATLAS and CMS is efficient in suppressing the soft background, it unavoidably introduces bias to jet measurements. On the other hand,

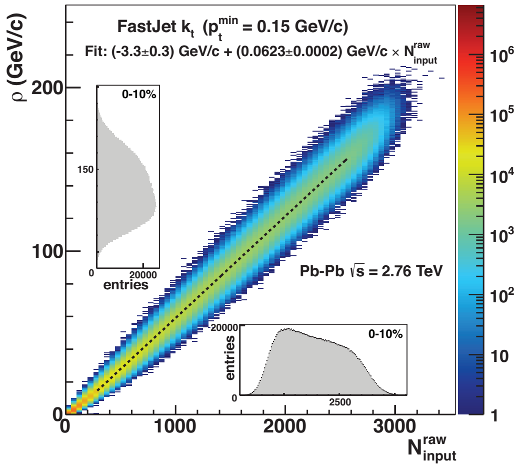

Figure 3.1: Dependence of charged particle background p_T density ρ on uncorrected multiplicity of charged tracks used for jet finding ($|\eta| < 0.9$) in Pb+Pb collisions at $\sqrt{s_{\rm NN}} = 2.76$ TeV. The insets show the projected distributions of ρ and raw multiplicity for the 10% most central Pb+Pb collisions. Figure is taken from [96].

the choice of the ATLAS and CMS experiments at the LHC in combination with their larger coverage in rapidity, allows to reconstruct jets with large radii (up to $R = 1$), while ALICE and STAR are limited by both their pseudorapidity acceptance and the low-$p_{\rm T}$ constituent cut-off to reconstruct jets with the radii of about 0.4. We note that here modern machine learning methods, could help to keep the jet $p_{\rm T}$ constituent bias as low as possible while being able to increase the radii of reconstructed jet. The interested reader is referred to recent ALICE measurements where for the first time it was possible to extract inclusive jet spectra in Pb+Pb collisions with the radii of 0.6 while still keeping low-$p_{\rm T}$ threshold on jet consituents [97]. In future, it will be certainly interesting to take similar approach also at RHIC energies and extend jet measurements to larger radii.

3.2 Measurements of dijet asymmetries

Measurements of dijet asymmetries by the ATLAS and CMS collaborations at the LHC for the first time clearly demonstrated the jet quenching effect in the QCD matter using fully reconstructed jets and marked thus the beginning of the precision jet era studies. Figure 3.2 shows an example of an event display of a highly asymmetric dijet event measured by the ATLAS experiment at the CERN LHC in central Pb+Pb collisions at $\sqrt{s_{NN}} = 2.76$ TeV [98]. One jet with transverse energy $E_T > 100$ GeV is clearly seen and there is no evident recoiling jet on the opposite side but one can observe high energy deposits in calorimeter cells distributed over a wide azimuthal region. To quantify the observed momentum imbalance between the transverse energies of the leading and sub-leading jets, dijet asymmetry observable $\rm A_J$ is defined as

$$A_J = \frac{p_{\rm T,1} - p_{\rm T,2}}{p_{\rm T,1} + p_{\rm T,2}} \,, \tag{3.1}$$

where the subscript 1 (2) refers to the leading (sub-leading) jet and consequently A_J is positive by construction.

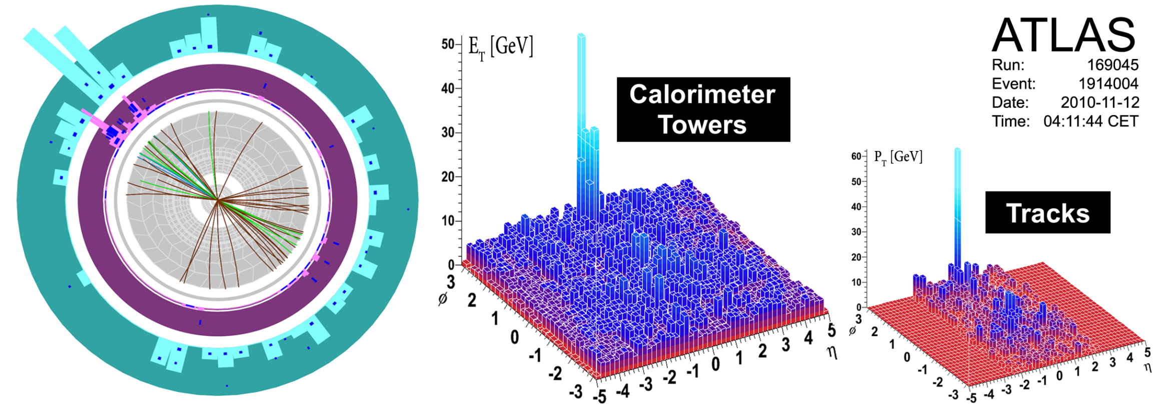

Figure 3.2: ATLAS event display of a highly asymmetric dijet event, with one jet with $E_T > 100$ GeV and no evident recoiling jet, and with high energy calorimeter cell deposits distributed over a wide azimuthal region. Figure is taken from [98].

Figure 3.3 shows the measured $\mathrm{A_J}$ distributions (top row) as well as distribution of $\Delta\phi$, the azimuthal angle difference between the two jets (bottom row), as a function of centrality in Pb+Pb collisions. The leading jet is required to have a transverse energy $E_{T,1} > 100$ GeV, and the second jet is the highest transverse energy jet in the opposite hemisphere with $E_{T,2} > 25$ GeV. The dijet imbalance in Pb+Pb collisions grows with collision centrality and the sub-leading jet gets increasingly attenuated, leading in some cases to highly asymmetric dijet events not observed in p+p data which are well described by simulation. The $\Delta\phi$ distributions show that although the leading and second jets are primarily back-to-back across all centralities studied, a systematic increase in the rate of second jets is observed at large angles relative to the recoil direction with increasing collision centrality.

A closer look at the LHC data revealed that there is an excess of low-p_{T} particles upto large distances from the jet axis and this excess is accompanied with a suppression of high-p_{T} particles. To quantitatively demonstrate this observation, the CMS experiment at the LHC calculated projection of missing p_{T} of reconstructed charged particle tracks onto the leading jet axis in Pb+Pb collisions [99]

$$\not{p}_{\mathrm{T}}^{\parallel} = \sum_{\mathrm{i}} -p_{\mathrm{T}}^{\mathrm{i}} \cos\left(\phi_{\mathrm{i}} - \phi_{\mathrm{Leading\ Jet}}\right), \tag{3.2}$$

where the sum was taken over all tracks with $p_{\mathrm{T}} > 0.5$ GeV/c and pseudo-rapidity $|\eta| < 2.4$. The event averaged $\langle \not{p}_{\mathrm{T}}^{\parallel} \rangle$ and its $\mathrm{A_J}$ dependence is shown in Figure 3.4 for two centralities and five transverse momentum ranges from 0.5–1 GeV/c to $p_{\mathrm{T}} > 8$ GeV/c. The data show that a large negative contribution to the missing p_{T} for the $p_{\mathrm{T}} > 8$ GeV/c range is balanced by the contributions from the lower-p_{T} regions. CMS also studied the radial dependence of the missing p_{T} separately for tracks inside and outside cones of size $\Delta R = 0.8$ around the leading and subleading jet axes (cf. [99]). The data manifest an in-cone imbalance of -20 GeV/c for the $\mathrm{A_J} > 0.33$ selection that is balanced by a corresponding out-of-cone imbalance of $\approx +20$ GeV/c that is carried mainly by charged particle tracks with low transverse momenta, $0.5 < p_{\mathrm{T}} < 4$ GeV/c. These measurements of highly unbalanced jets in central Pb+Pb

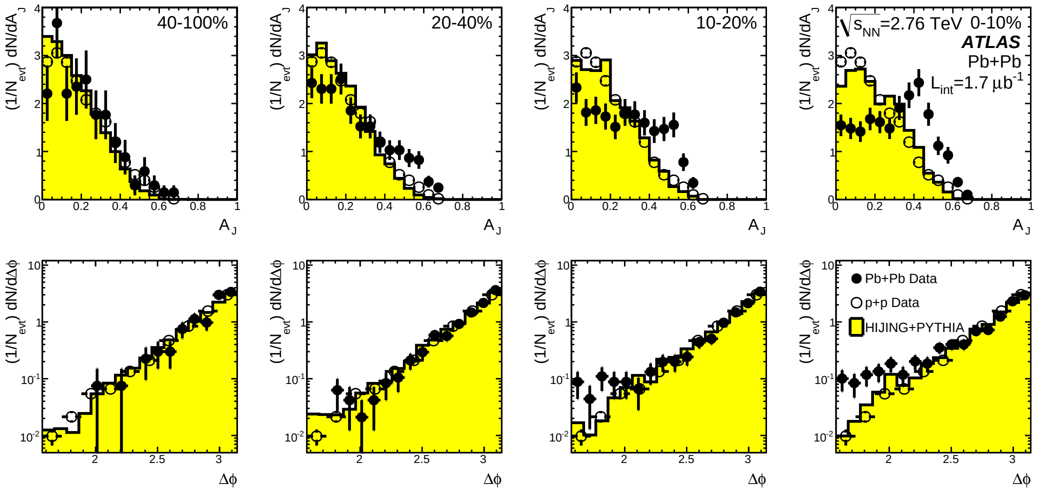

Figure 3.3: (Top row) Dijet asymmetry (A_J) distributions in Pb+Pb collisions at $\sqrt{s_{NN}}$ = 2.76 TeV (points) and unquenched HIJING Monte-Carlo simulations with superimposed PYTHIA simulated dijets (solid yellow histograms), as a function of collision centrality (left to right from peripheral to central events). Proton-proton data from $\sqrt{s}$ = 7 TeV is shown as open circles. (Bottom row) Distribution of $\Delta\phi$, the azimuthal angle between the two jets, for data and HIJING+PYTHIA, also as a function of centrality. Figure is taken from [98].

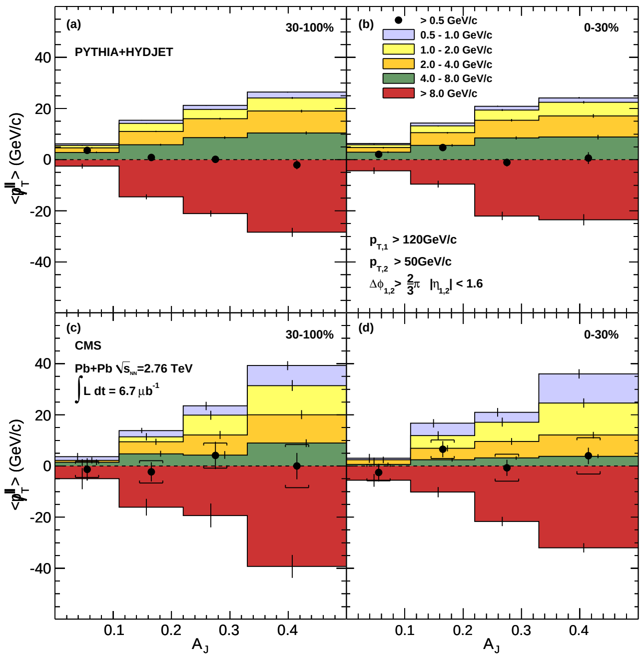

Figure 3.4: Average missing transverse momentum for tracks with $p_T > 0.5$ GeV/c, projected onto the leading jet axis (solid circles) as a function of dijet asymmetry A_J in Pb+Pb collisions at $\sqrt{s_{NN}}$ = 2.76 TeV for 30–100% centrality (left) and 0–30% centrality (right) for PYTHIA+HYDJET simulations (top row) and data (bottom row), respectively. Colored bands show the missing p_T contribution for five ranges of track p_T. Figure is taken from [99].

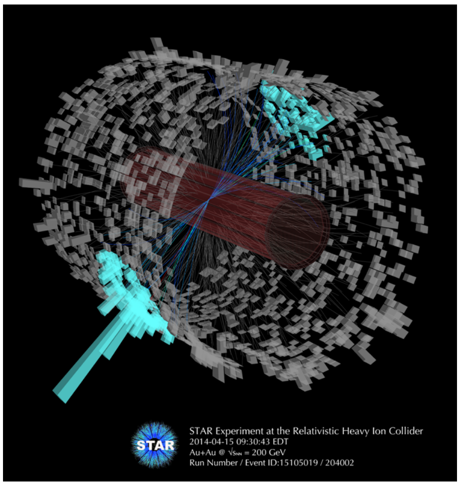

Figure 3.5: STAR event display of a central (head-on) Au+Au collision at $\sqrt{s_{NN}}$ = 200 GeV with back-to-back jets.

collisions at the LHC energy are consistent with jet quenching scenario in the produced QCD matter and provided quantitative input to models of the transport properties of the medium.

3.3 Inclusive jet production

In contrast to di-jet asymmetry measurements, for an inclusive jet measurement to be theoretically interpretable, one must have a well-defined jet population arising from hard processes. This requires to exclude the yield of purely combinatorial jet candidates having contributions only from soft processes, and disentangle the effects of overlapping primordial jets arising from hard processes. To suppress the uncorrelated background yield, both ALICE and STAR, apply a cut on the leading particle of each jet candidate, $p_{\mathrm{T,lead}} > p_{\mathrm{T,lead}}^{\mathrm{min}}$. This approach obviously imposes a bias on the fragmentation pattern of the measured jet population and therefore the jet population is "quasi-inclusive". On one hand, the value of $p_{\mathrm{T,lead}}^{\mathrm{min}}$ must be sufficiently high that probability for multiple hadrons to satisfy this cut in a central heavy-ion collision is negligible. On the other hand, the $p_{\mathrm{T,lead}}^{\mathrm{min}}$ value should be as low as possible, to minimize the bias imposed on the accepted jet population.

The modification of inclusive jet production in medium is commonly quantified by comparing measurements in central heavy-ion collisions to those in smaller systems in which QGP formation over a large volume is not expected to occur, either p+p collisions or peripheral heavy-ion collisions. We can therefore, in a full analogy with Eq. 3.4 introduced for inclusive particle production, define the respective nuclear modification factors for inclusive jet production replacing the measured yields of particles with those of jets.

We first discuss measurements of the central-to-peripheral R_{CP} factor in which the reference spectrum is measured in peripheral heavy-ion collisions:

$$R_{\mathrm{CP}} = \frac{\frac{1}{N_{\mathrm{events}}^{\mathrm{cent}}} \cdot \frac{d^2 N_{\mathrm{cent}}}{dp_{\mathrm{T,jet}} d\eta}}{\frac{1}{N_{\mathrm{events}}^{\mathrm{periph}}} \cdot \frac{d^2 N_{\mathrm{periph}}}{dp_{\mathrm{T,jet}} d\eta}} \cdot \frac{\langle N_{\mathrm{bin}}^{\mathrm{periph}} \rangle}{\langle N_{\mathrm{bin}}^{\mathrm{cent}} \rangle}. \tag{3.3}$$

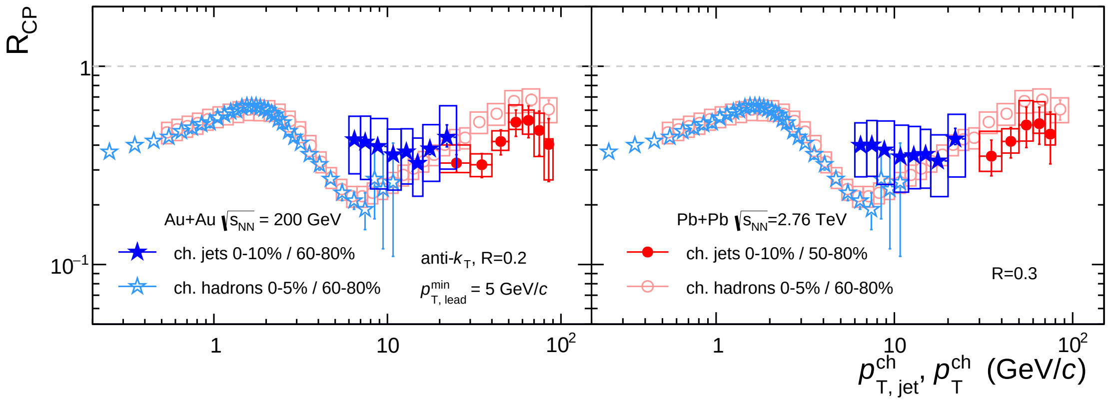

Figure 3.6: R_{CP} distributions of charged-particle jets from Fig. **??** compared to the ALICE measurement in Pb+Pb collisions at $\sqrt{s_{\mathrm{NN}}} = 2.76$ TeV [100], for $R = 0.2$ (left) and $R = 0.3$ (right). Also shown are R_{CP} values for inclusive charged hadrons in Au+Au collisions at $\sqrt{s_{\mathrm{NN}}} = 200$ GeV [67] and in Pb+Pb collisions at $\sqrt{s_{\mathrm{NN}}} = 2.76$ TeV [84]. Figure is taken from [95].

Figure 3.5 shows an example of the event display with a jet signal as seen by the STAR experiment in Au+Au collisions at $\sqrt{s_{NN}} = 200$ GeV. The first fully corrected R_{CP} distributions of charged-particle jets at RHIC energy wer obtained only recently [95]. The R_{CP} values shown in Figure 3.6 reaches values of about 0.4 for all measured R parameters with essentially no dependence on jet p_{T}. Comparing this R_{CP} measurement with that in Pb+Pb collisions measured by the ALICE experiment at $\sqrt{s_{\mathrm{NN}}} = 2.76$ TeV [100] and also with the R_{CP} for inclusively produced charged hadrons [67,84], the observed independence of charged-particle jet R_{CP} on $p^{\mathrm{ch}}_{\mathrm{T,jet}}$ is in contrast to the significant p_{T} dependence of charged-hadron nuclear modification factor. The inclusive charged-hadron distribution at high p_{T} arises predominantly from the leading hadron of the corresponding jet. The correlation between hadron p_{T} and its parent jet p_{T} has a distribution that reflects fluctuations in the fragmentation process which may consequently lead to a different p_{T} dependence of R_{CP} for hadrons and jets. What is however remarkable is that both the values of charged-hadron R_{CP} at RHIC and the LHC as well as the charged-particle jet R_{CP} at RHIC and the LHC are consistent within uncertainties. Naively one would expect the suppression for jets to be smaller than for hadrons, since multiple jet fragments should be collected into the jet cone and recover some of the medium-induced fragmentation. This observation indicates that the ‘lost’ momentum is redistributed to angles larger than $R = 0.3$ by interactions with the medium. The comparison of hadron and jet suppression which spans a large interval in the collision energies from RHIC to the LHC provides important and new constraints on theoretical understanding of jet quenching.

Let us next discuss the inclusive jet R_{AA}

$$R_{\mathrm{AA}} = \frac{\frac{1}{N_{\mathrm{events}}} \cdot \frac{d^2 N_{\mathrm{AA}}}{dp_{\mathrm{T,jet}} d\eta}}{T_{\mathrm{AA}} \cdot \frac{d^2 \sigma_{\mathrm{p+p}}}{dp_{\mathrm{T,jet}} d\eta}}, \tag{3.4}$$

starting again with results from RHIC. Due to the unavailability of the charged-particle p+p

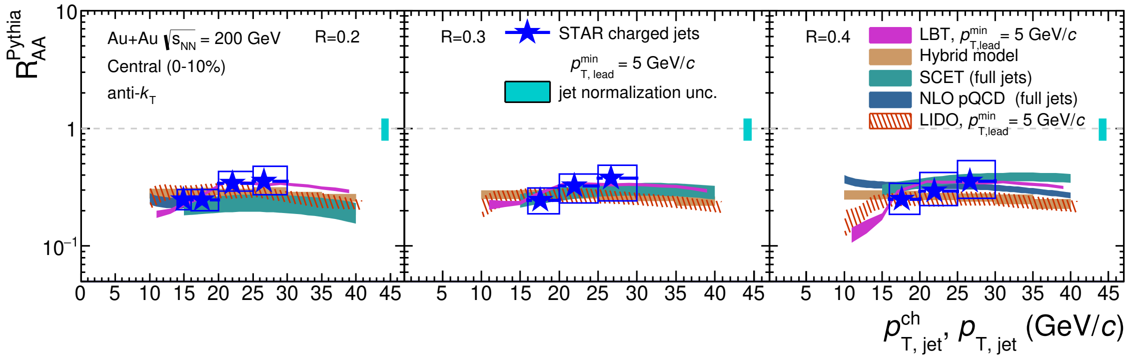

Figure 3.7: Comparison of charged-particle jet R_{AA}^{Pythia} in Au+Au collisions at $\sqrt{s_{NN}}$ = 200 GeV (stars) to theoretical calculations for full jets labeled as NLO [104], SCET [73,105], Hybrid Model [106] and LIDO [107]. Only points from the region where the bias in the data due to the $p_{\text{T,lead}}^{\text{min}}$ cut is small are shown. Figure is taken from [95].

jet spectra for studied kinematic selections, the PYTHIA Monte-Carlo generator 6.428 [101, 102] has been used instead. Figure 3.7 shows the R_{AA} for charged-particle jets in central Au+Au collisions for three different jet radii, R = 0.2, 0.3 and 0.4, respectively. No $p_{\text{T,lead}}^{\text{min}}$ cut is imposed on the reference PYTHIA jet population to not introduce further bias into the measurement as the bias may differ in p+p and Au+Au collisions. As can be see also for this nuclear modification factor, the R_{AA} of charged-particle jets is strongly suppressed and consistenly falls into the suppression trend of inclusive charged hadrons [67, 103] and neutral pions [81].

At the LHC energies, $\sqrt{s_{NN}}$ = 2.76 TeV and 5.02 TeV, the jet R_{AA} in central Pb+Pb collisions also exhibits a strong suppression. The ALICE results [108] shown in Figure 3.8 cover predominantly the low jet p_{T} range ($<$ 100 GeV/c) where the jet suppression is strongest. We can compare the ALICE jet R_{AA} also with the available measurements by the ATLAS [109] and CMS [82] collaborations. The ATLAS and CMS jet R_{AA} values are in the overlap p_{T} region in a good agreement with those from ALICE. Overall, from this comparison it can be concluded that the LHC data do not manifest any significant dependence on the resolution parameter R, nor any $\sqrt{s}$ dependence of the jet R_{AA} within current uncertainties. What is however peculiar is the fact that the jet R_{AA} even for the very high energetic jets accessible by ATLAS and CMS still shows the suppression in central Pb+Pb collisions relative to the p+p data. Moreover, as recent measurements by ATLAS [110] and CMS [111] revealed, the R_{AA} values remain smaller than unity even if jets are reconstructed with the resolution parameter R = 1.0 as can be seen on Figure 3.9.

Let us now compare the inclusive jet suppression to recent theoretical calculations incorporating jet quenching:

- JEWEL [112,113] is a Monte Carlo generator including the BDMPS jet energy loss with a parton shower. It allows for the recoiling thermal medium particles to be included in the jet energy (“recoil on”), or to let them free stream and do not interact again with the medium (“recoil off”).

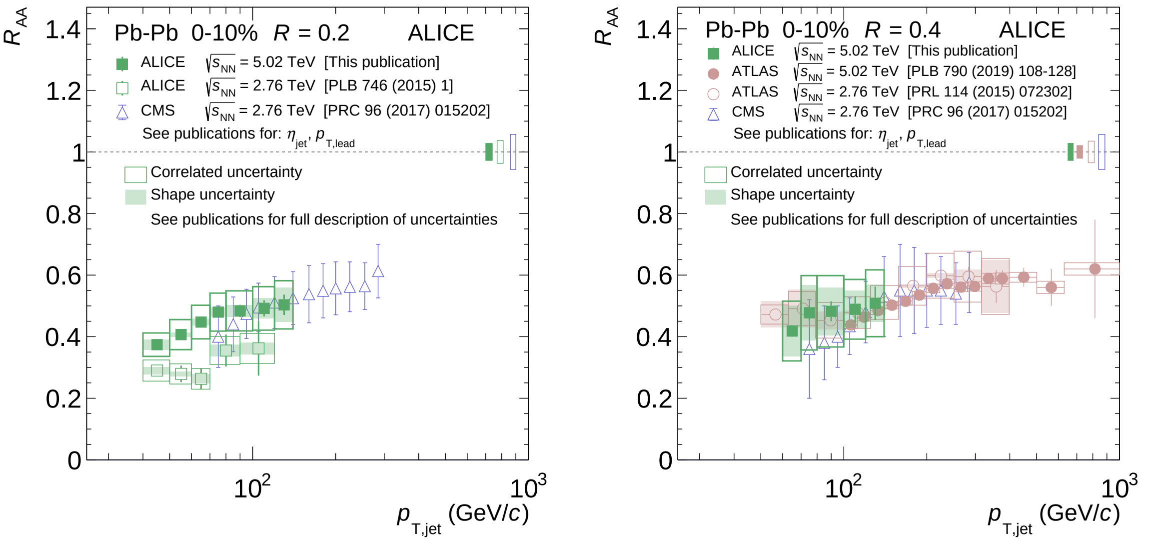

Figure 3.8: Jet R_{AA} in central Pb+Pb collisions at LHC energies for $R = 0.2$ (left) and $R = 0.4$ (right) for all currently published experimental results. Closed markers denote $\sqrt{s} = 5.02$ TeV, and open markers denote $\sqrt{s} = 2.76$ TeV. For ALICE, a leading track requirement is imposed in the p+p reference. Figures are taken from [108].

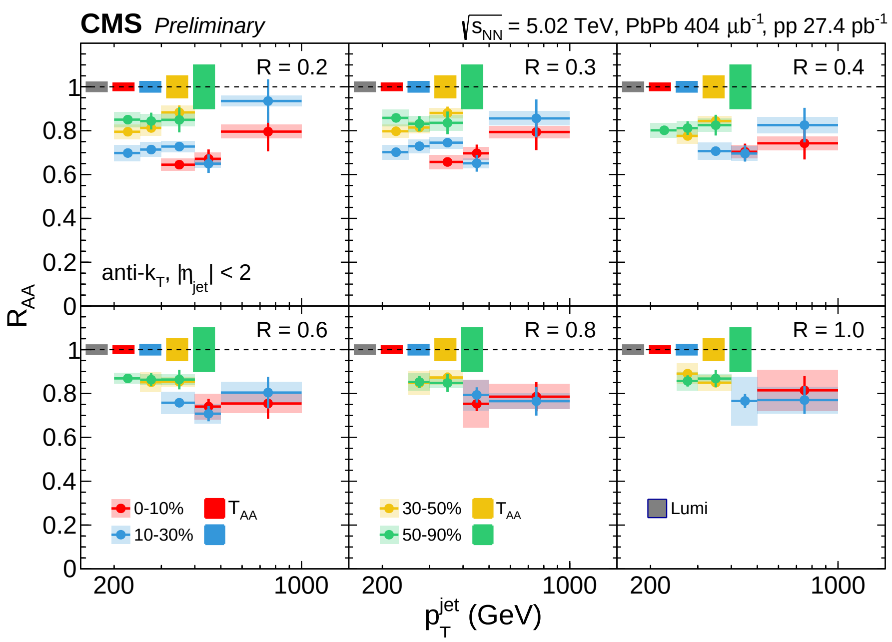

Figure 3.9: Full-jet R_{AA} as a function of jet p_{T} for various R and centrality classes in Pb+Pb collisions at $\sqrt{s_{NN}} = 5.02$ TeV by CMS. Figure is taken from [111].

- Next-to-leading order (NLO) pQCD calculation from [104] that accounts for initial-state nuclear modification [114, 115] and incorporates collisional partonic energy loss in the QGP calculated using a weak-coupling approach.

- Linear Boltzmann Transport (LBT) model [116, 117] implements pQCD energy loss based on a Higher Twist gluon radiation spectrum induced by elastic scattering. LBT describes the evolution of jet and recoiling medium particles through the thermal medium with linear Boltzmann equations. An effective strong coupling constant α_s is taken as a free parameter to fit experimental data.

- Soft Collinear Effective Theory with Glauber gluons (SCET$_G$) [118–121] is based on the approach of soft collinear effective theory (SCET) in which the jet cross-section is factorized into the initial hard scattering and a "jet function" corresponding to the fragmentation of a hard-scattered parton into a jet. In SCET$_G$, jet energy loss in medium is implemented by interactions of jet partons with the medium in an effective field theory via the exchange of "Glauber" gluons.

- Hybrid Model [74, 106, 122, 123] combines several processes governing the evolution and interaction of jet showers in the medium. The production and evolution of the jet shower uses a weakly-coupled approach based on PYTHIA, while the interaction of shower partons with the QGP uses a strongly-coupled holographic approach based on $N = 4$ supersymmetric Yang-Mills theory. Hybrid Model also includes p_{T} broadening of the shower in the QGP, and back-reaction of the medium due to passage of the jet. The scale at which the medium can resolve two split partons is provided by the parameter L_{res}, and the medium evolution is modeled by a hydrodynamic expansion.

- LIDO model [107] is based on a modified formulation of semi-classical Boltzmann transport using pQCD cross sections with running α_S and an approximate treatment of in-medium multiple-scattering coherence. Medium excitation is included using a linearized approximation to the hydrodynamic equations. The LIDO model reproduces inclusive hadron and jet R_{AA} suppression at the LHC. The LIDO calculations presented here for the RHIC energy correspond to variation of the temperature-dependent coupling constant scale parameter between 1.5–2.0 πT.

For more details on the particular theoretical model we kindly refer the reader to the original publications.

At the LHC, model calculations shown in Figure 3.10 exhibit strong suppression and qualitatively reproduce the weak dependence of R_{AA} of jet p_{T} although the predictions differ quantitatively. For the small resolution parameter, $R = 0.2$, JEWEL significantly underpredicts the data even for medium recoils included. The fact that there is a small difference between recoils on/off options is related to the fact that for smaller radii the impact from medium recoil is smaller. For larger R, $R = 0.4$, including medium recoils leads to better description of the data. The LBT calculation shows a better agreement with the data, although we note that there is a tension with the data. Better description of the data is achieved for the SCET$_G$ calculation as well as the Hybrid model, although a slight tension below p_{T} of 100 GeV/c exists for the Hybrid model as well. Inspecting the shapes of the R_{AA} on jet p_{T}, the dependence of SCET$_G$ is different from the rest of the available calculations. The comparison with the data also show, that it will be important to extend the jet R_{AA} measurement to larger R values as the model predictions seem to span a wider range in R_{AA} with increasing R.

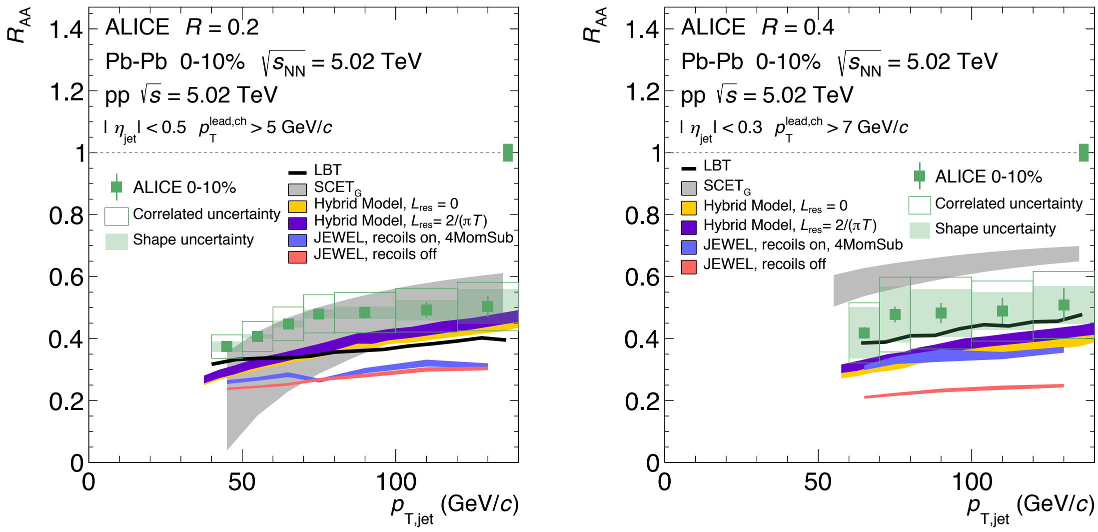

Figure 3.10: Jet $R_{\rm AA}$ at $\sqrt{s_{NN}}$ = 5.02 TeV for $R = 0.2$ (left) and $R = 0.4$ (right) compared to model predictions (see text). The combined T_{AA} uncertainty and p+p luminosity uncertainty of 2.8% is illustrated as a band on the dashed line at $R_{\rm AA} = 1$. Figures are taken from [108].

At RHIC, the measured charged-particle jet $R_{\rm AA}$ is compared with available model calculations in Figure 3.7. We note that the Hybrid, LBT, and LIDO calculations were carried out for charged-particle jets, while the SCET and NLO pQCD calculations are for fully reconstructed jets. However, as the $p_{\rm T}$ dependence of $R_{\rm AA}$ is week, the comparison is meaningul. The LBT and LIDO calculations also include a cut on the leading constituent hadron of 5 GeV/c as applied in the data. As can be observed all these calculations are consistent within current uncertainties with the measured inclusive jet $R_{\rm AA}$. The largest differences between models are observed for $R = 0.4$ and therefore future measurements of jet $R_{\rm AA}$ with improved systematic precision and larger resolution parameters may be able to discriminate between these models at RHIC energy.

Overall, these model comparisons show that investigation of complementray jet observables acrross the collision energies and their global analyses is important to confront the model predictions but also the theoretical community needs to standardize its approach to in-medium energy loss as for example performed recently within the JETSCAPE collaboration [124].

3.4 Semi-inclusive hadron-jet production

As next observable related to jet tomography of the QCD medium, let us discuss measurements of jets recoiling from a hard trigger particle. This observable offers a unique approach to jet quenching studies in addition to the jet measurements presented above. Exploration of suppression of recoiling jet yields for a given resolution parameter R in central heavy-ion collisions gives access to energy transported to angles larger than R and ratios of yields at different R values enable measurements of medium-induced modification of jet shape (intra-

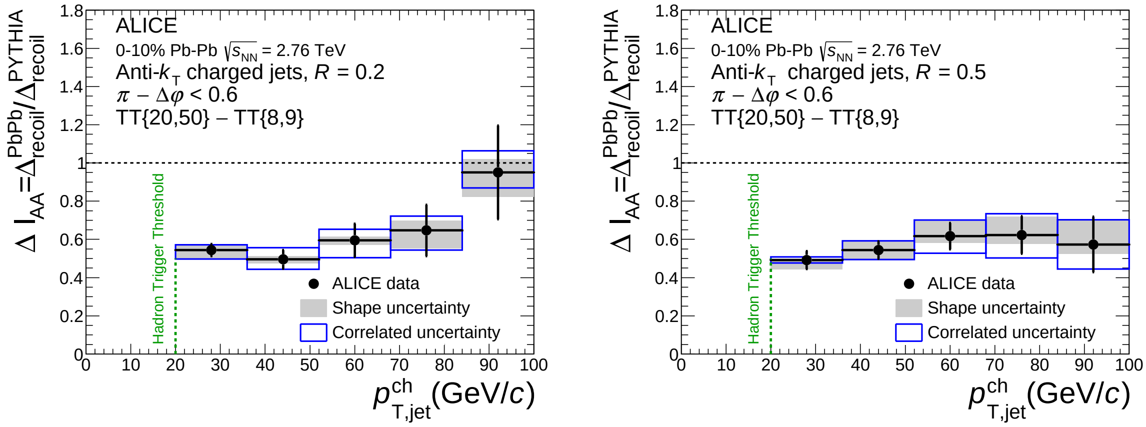

Figure 3.11: ΔI_{AA} of recoil charged-particle jets in central Pb+Pb collisions at $\sqrt{s_{NN}}$ = 2.76 TeV measured by ALICE, for R = 0.2 and 0.5. The p+p reference is calculated in PYTHIA. Figures are taken from [127].

jet broadening). The inter-jet broadening and related acoplanarity can be approached via azimuthal distributions of recoiling jets relative to a trigger hadron. The acoplanarity of lower energy jets is predicted to be sensitive to $\langle \hat{q} \cdot L \rangle$, where $\hat{q}$ is the jet transport parameter in medium and L is the path-length traversed by a parton in the medium. Last but not least, enhanced jet yield in the tail of the $\Delta\phi$ distribution could originate from medium-induced Molière scattering off quasiparticles in the hot QCD matter [125, 126].

We note that first studies of the azimuthal distributions of jets recoiling from a high-p_{T} hadron were performed by ALICE [127] and STAR [128], but these measurements had limited accuracy. In 2020, using high-statistics Run-2 data ALICE released preliminary results [129] from Pb+Pb collisions at $\sqrt{s_{\mathrm{NN}}} = 5.02$ TeV which show that the $\Delta\phi$ distribution for $R = 0.5$ jets is narrower in central Pb+Pb relative to PYTHIA simulations. Future measurements using high statistics measured p+p data in combination with an extension to larger R and jet p_{T} values will provide definite conclusion on presence of quasi-particles in hot and dense matter at the LHC.

Let us know focus on the nuclear modification factor of the recoiling charged-particle jet yields, which are labeled as I_{AA} and I_{CP}, respectively. Figure 3.11 shows the I_{AA} in Pb+Pb collisions at $\sqrt{s_{\mathrm{NN}}} = 2.76$ TeV measured by ALICE for the resolution parameter $R = 0.2$ and $R = 0.5$ [127]. Due to the lack of sufficient statistics of the p+p data at $\sqrt{s} = 2.76$ TeV, a PYTHIA reference was used instead. The ALICE data shows a significant suppression of recoiling jet yield relative to PYTHIA by up to a factor two for the studied range of R. These results indicate that the in-medium energy loss arises predominantly from radiation at angles larger than 0.5. The yields of recoiling charged-particle jets and their nuclear modification factor in Au+Au collisions at the top RHIC energy of $\sqrt{s_{\mathrm{NN}}} = 200$ GeV for $R = 0.2$ and 0.5 measured by STAR are displayed in Figure 3.12. In STAR, due to the lack of the p+p reference spectrum, data from peripheral Au+Au collisions were used and the modification of the recoiling charged-particle jet yields is thus expressed by the corresponding central-to-peripheral ratio I_{CP}. Similarly as at the LHC, there is a large suppression of recoiling jet yields measured at RHIC and the observed suppression is even somewhat stronger. For

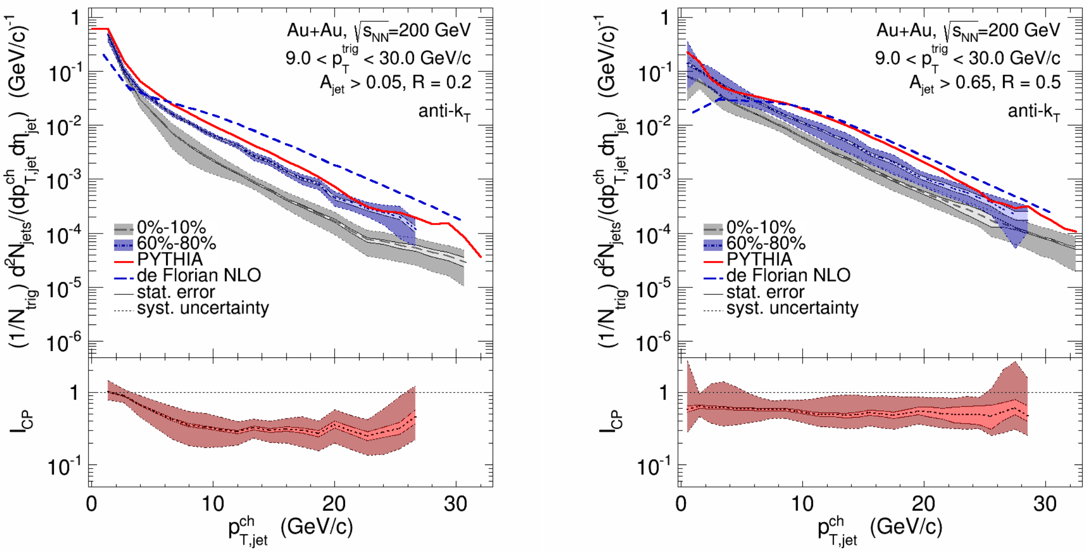

Figure 3.12: Distributions of recoil charged-particle jet yields (upper panels) and their ratio $I_{\rm CP}$ (lower panels) for central and peripheral Au+Au collisions at $\sqrt{s_{NN}}$ = 200 GeV, for jets with $R = 0.2$ and 0.5. The upper panels also show the recoil jet yields for p+p collisions calculated in PYTHIA at the charged-particle level and NLO pQCD transformed to the charged-particle level. Figures are taken from [128].

completeness, Figure 3.12 also contains PYTHIA and pQCD at NLO calculations. The central value of the PYTHIA distribution is about 20% above the peripheral Au+Au data for all resolution parameters studied. For $R = 0.2$ the NLO distribution is even higher than PYTHIA and a better agreement is observed for larger R values. This observation is similar to that discussed above for p+p data at $\sqrt{s} = 7$ TeV.

3.5 Medium induced jet broadening

Next we turn our attention to the medium induced jet broadening which can be simply studied by calculating ratios of inclusive or semi-inclusive recoiling jet cross sections at different values of R. Ratios of jet cross sections are of particular interest for measuring the transverse jet energy profile and its modification due to jet quenching since there is significant cancellation of systematic uncertainties in the ratio, both experimenally [130, 131] and theoretically [106, 132, 133].

The ratio of inclusive jet cross sections [130, 131, 134] as well as those of semi-inclusive recoil jet yields [127] in p+p collisions are less than unity and were found to be consistent with pQCD calculations at NLO and NNLO (Next-to-Next-to-Leading-Order) [132, 133, 135] and can be used as a reference measurements for heavy-ion collisions. Figure 3.13 displays the ratio of charged-particle jet inclusive cross sections for two different R parameters, $\sigma(R = 0.2)/\sigma(R = 0.3)$ for central and peripheral Pb+Pb collisions at $\sqrt{s_{\rm NN}} = 2.76$ TeV [100]. The comparison of the measured ratio with PYTHIA simulations at particle level shows that the measured transverse charged-particle jet shape is consistent with that in vacuum even for central Pb+Pb collisions and no sign of modified jet structure is observed for the resolution

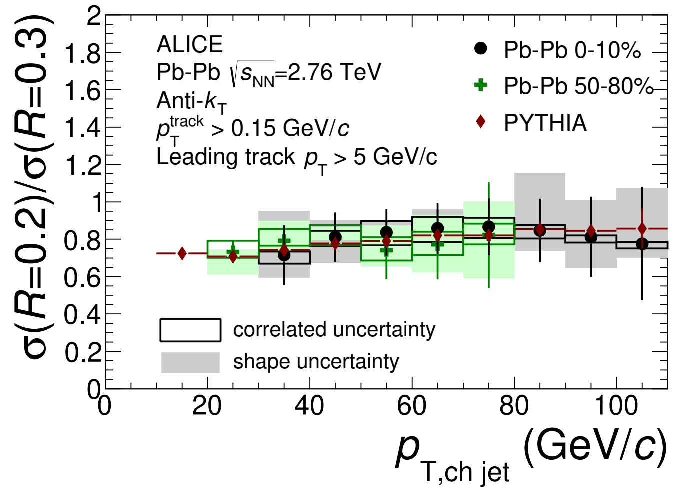

Figure 3.13: Ratio of charged-particle jet p_T spectra with the resolution parameter $R = 0.2$ and 0.3 and the leading charged particle $p_{T,lead}^{min} = 5$ GeV/c in Pb+Pb collisions at $\sqrt{s_{NN}}$ = 2.76 TeV and simulated PYTHIA p+p events. Figure is taken from [100].

parameters studied within uncertainties.

Moving to lower collision energy of RHIC, in Au+Au collisions at $\sqrt{s_{NN}} = 200$ GeV [95], the ratio of charged-particle jet inclusive cross sections has been measured for the resolution parameters $R = 0.2$ and 0.4 and is shown in Figure 3.14 for central and peripheral Au+Au collisions. The measured ratio is again less than unity for both centralities as expected. The data are also confronted with calculations for p+p collisions from PYTHIA and HERWIG Monte-Carlo simulators, which agree within uncertainties with the measured ratios in Au+Au

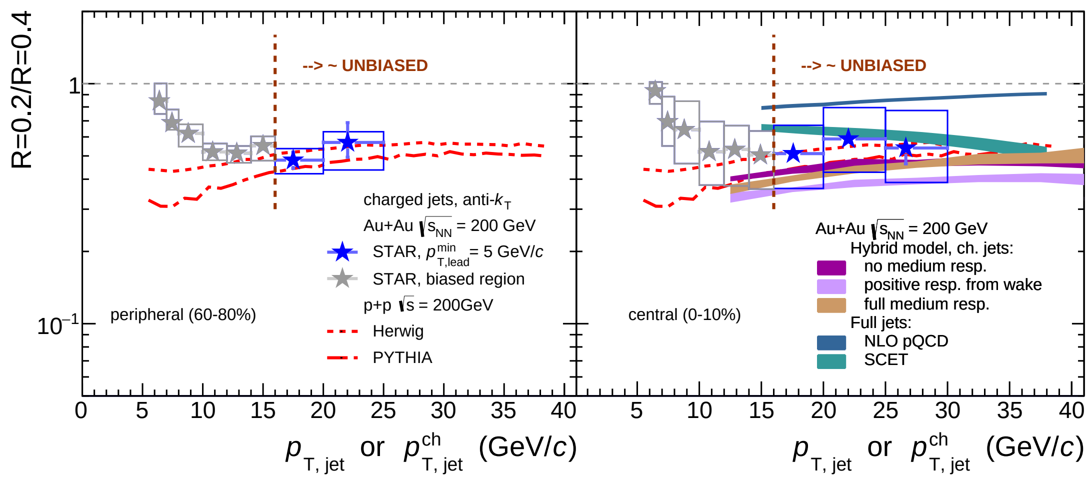

Figure 3.14: Ratio of charged-particle jet yields for $R = 0.2$ and 0.4, for peripheral (left) and central (right) Au+Au collisions at $\sqrt{s_{NN}} = 200$ GeV and $p_{T,lead}^{min} = 5$ GeV/c. The data are compared with PYTHIA [101], HERWIG [136] and theoretical predictions for fully-reconstructed jets in Au+Au collisions. The region where the bias due to the $p_{T,lead}^{min}$ cut is small is indicated by the vertical dashed line. Figure is taken from [95].

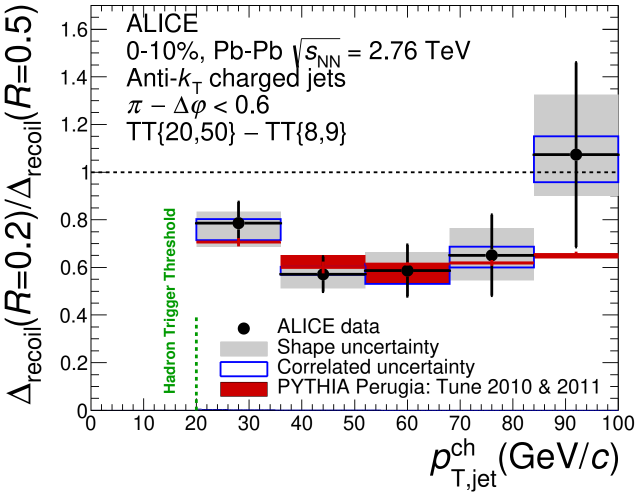

Figure 3.15: Ratio of Δ_{recoil} for $R = 0.2$ and 0.5 for central Pb+Pb and p+p collisions simulated in PYTHIA at $\sqrt{s} = 2.76$ TeV. Figure is taken from [127].

collisions. This indicates that also at the RHIC energy and for larger $R = 0.4$ there is no significant modification of the transverse jet profile due to quenching in central Au+Au collisions. Besides Monte-Carlo generators for p+p collisions we also compare the data with predictions of the SCET and Hybrid models as well as NLO calculation discussed already above in the context of the inclusive jet R_{AA} measurements. The SCET and Hybrid Model predictions agree with the measurement within uncertainties. Although each of these two models predicts different p_{T} dependence of the ratio, the current experimental uncertainties cannot discriminate between them. In contrast, the NLO calculation predicts a larger ratio, not consistent with the data within uncertainties. It is important to point out that the observation of the medium induced jet broadening from the inclusive jet spectra ratio is in contrast with measurements of di-jet asymmetry $\mathrm{A_J}$ at RHIC [137]. These measurements found that energy lost due to quenching for jets with $R = 0.2$ is largely recovered for jets with $R = 0.4$, indicating thus a significant medium-induced modification of the transverse profile for the jet population selected in [137]. However, this population differs significantly from the jet population in the inclusive jet analysis. Interpretation of the observed differences in both analyses in terms of transverse jet profile modification requires therefore modeling of both measurements in a common theoretical framework (e.g. [138]).

Let us now discuss the medium modification of jet shape in semi-inclusive recoil-jet population based on the hadron+jet results presented above. Figure 3.15 shows the ratio of the recoil-jet yield p_{T} distributions for $R = 0.2$ and 0.5 in central Pb+Pb collisions at $\sqrt{s_{NN}}$ = 2.76 TeV from ALICE [127]. The data in central Pb+Pb collisions are within uncertainties in agreement with PYTHIA predictions which points to the fact that the intra-jet energy profile is not changed significantly for $R \leq 0.5$. We also note that the low momentum infrared cutoff for jet constituents (0.15 GeV/c) imposes significant constrains on the correlated energy within the jet cone that would not be detected. Figure 3.16 displays similar measurements performed in STAR [128], where the recoil-jet yield p_{T} distributions and their ratios are shown separately for peripheral and central Au+Au collisions at $\sqrt{s_{NN}}$ = 200 GeV. Sim-

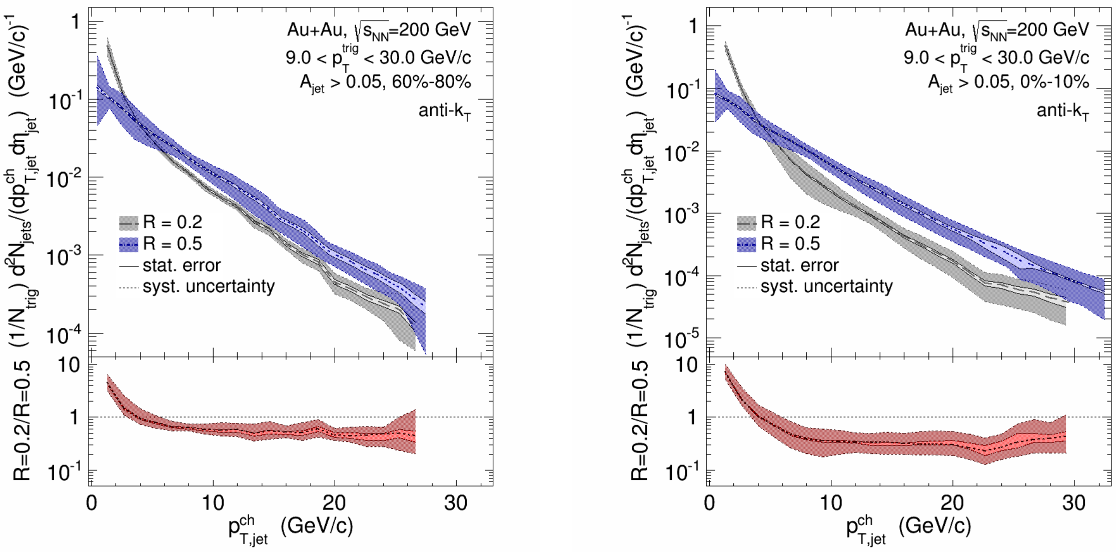

Figure 3.16: Ratio of Δ_{recoil} for $R = 0.2$ relative to $R = 0.5$ for peripheral (left) and central Au+Au (right) collisions at $\sqrt{s_{NN}} = 200$ GeV. Figures are taken from [128].

ilarly as at the LHC energy, also at RHIC the measured ratio of recoiling charged-particle jet yields is less than unity reflecting the intra-jet distribution of energy transverse to the jet axis. Comparison of central and peripheral collisions shows no evidence of broadening of the jet shower due to the jet quenching in medium. Although the hadron+jet measurements probe different jet populations and cannot be directly compared to other jet observables, we note that the ATLAS measurement [109] of inclusive jet yields in Pb+Pb collisions at the LHC reveals significant dependence on jet resolution parameter R from 0.2 to 0.5 for jet transverse momenta 40-100 GeV/c. This is also corroborated by the CMS measurement of the p_{T}-weighted jet shape distributions for dijets [139], where an enhancement for radial distances from the di-jet axis larger than 0.3 for the subleading jet ($p_{\mathrm{T}} > 50$ GeV/c) in central Pb+Pb relative to p+p collisions is observed.

As the inclusive and recoiling charged-particle jet spectra have approximately exponential shape, for a range of jet p_{T} in which the nuclear modification factors are constant, one can equivalently express the observed suppression as a horizontal shift in p_{T} between the reference jet distribution spectrum (p+p or peripheral one) and the jet distribution in central A+A collisions. This approach enables direct comparison of these two jet suppression measurements because it removes the effect of the jet spectrum shape. The p_{T}-shift values can be further interpreted as the population-averaged energy transport out of the jet cone due to quenching. Extracted values of the p_{T}-shift from the results presented in [95, 128] and further available data from RHIC such as inclusive π^0 spectra [81] and recent STAR measurements of π^0+jet and direct photon+jet correlations [140], as well as the LHC hadron+jet results [127] are displayed in Figure 3.17. The central values of the p_{T}-shift for the inclusive jet distributions are consistently smaller than those for recoiling jets at RHIC energy, but within current statistical and systematic uncertainties no significant difference is observed. Future analysis with significantly improved uncertainties may provide discrimination of the medium-induced

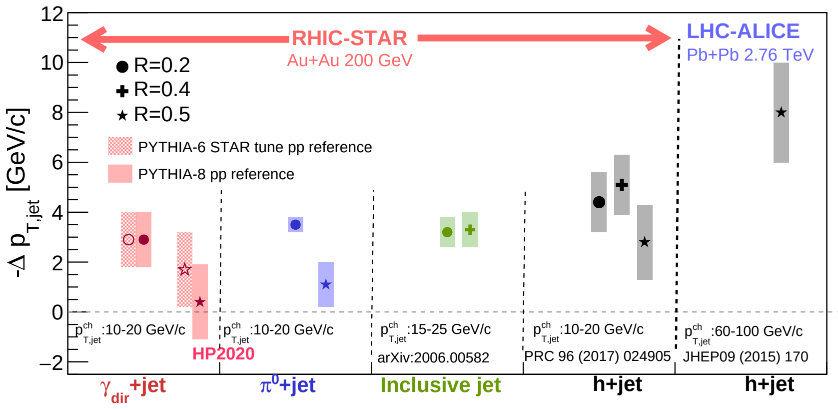

Figure 3.17: The p_{T} shift for γ_{dir}+jet,π^0+jet, inclusive jet, h+jet measurements at RHIC, and h+jet at the LHC. Note the different jet p_{T} ranges. Figure is taken from [140].

energy loss averaged over the inclusive and recoil jet populations. However, it is important to note that the path-length distribution of jets contributing to the two measurements compared may differ. Comparing the RHIC p_{T}-shift values with the LHC hadron+jet measurement, there is an indication of smaller in-medium energy loss at RHIC than at the LHC. As in both ALICE and STAR analyses jets include tracks with $p_{\mathrm{T}} > 0.2$ GeV/c, this p_{T} shift can be intepreted as the energy transported to radii larger than $R = 0.5$.

3.6 Strangeness production in jets

Next we present recent results on flavour composition of jets focusing on strangeness production in jets and underlying event in p+p, p+Pb and Pb+Pb collisions with the ALICE experiment. The aim is to investigate separately baryon-to-meson effects on particles produced in hard processes (i.e. in jets) and those produced in underlying event in order to resolve whether there are similar particle production mechanisms in high-multiplicity p+p and p+Pb as in heavy-ion collisions. Due to limited statistics, the measurements so far focused on strangeness production in jets using Λ and K^0_S and on data measured at the LHC. These so called V0 particles can be reconstructed from their decay products systematically exploring the characteristics of their weak decay topologies. In particular, the two-body decay channels $K^0_S \to \pi^+ + \pi^-$ and $\Lambda(\bar{\Lambda}) \to p + \pi^-(\bar{p} + \pi^+)$ are typically used.

To obtain the yield of V0 particles associated within a jet cone (JC), the V0 particles must be selected based on their distance from the jet centroid, R(V0; jet), in the pseudorapidity and azimuthal angle. The left panel of Figure 3.18 shows the corrected Λ/K^0_S ratios for particles associated with reconstructed charged-particle jets in high-multiplicity p+Pb collisions at $\sqrt{s_{\mathrm{NN}}} = 5.02$ TeV [141]. The Λ/K^0_S ratio in jets is clearly much smaller than the ratio of inclusively produced strange baryons and mesons. The data are qualitatively described by PYTHIA 8 simulations of p+p collisions. In the right panel of Figure 3.18 data from p+p collisions at $\sqrt{s} = 7$ TeV are displayed to explore whether there are possibly differences between the Λ/K^0_S associated with jets in p+Pb and p+p collisions. Due to the lack of available data at the same collision energy, the p+p study had to be performed at somewhat

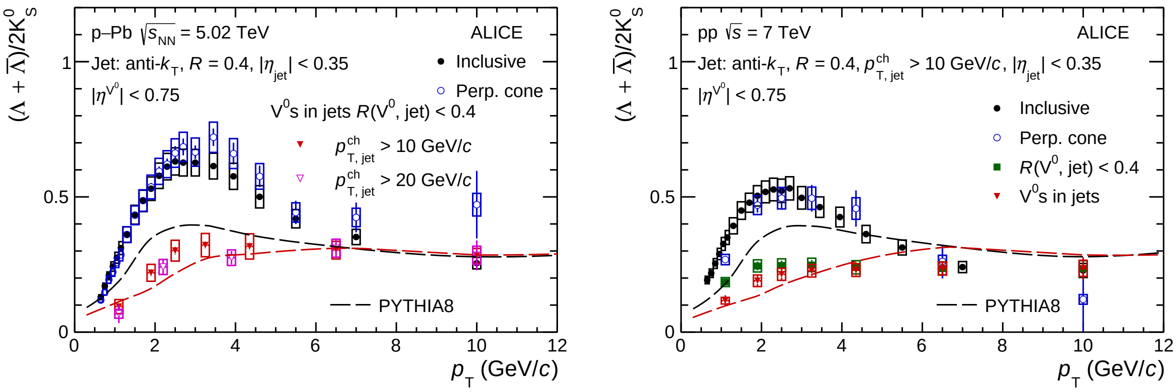

Figure 3.18: Λ/K^0_S ratio in p+Pb collisions at $\sqrt{s_{NN}}$ = 5.02 TeV (left) and p+p collisions at $\sqrt{s}$ = 7 TeV (right) as a function of strange particle p_{T}, associated with charged-particle jets together with that in inclusive and perpendicular cone selection, and jet cone selection in case of pp collisions. In both upper and lower panels, the dashed curves are from PYTHIA 8 simulations. Figures are taken from [141].

larger collision energy of $\sqrt{s_{NN}}$ = 7 TeV, but we do not expect any significant impact on physics message drawn from this comparison. Within current experimental uncertainties the strange baryon-to-meson ratio in jets in p+Pb collisions is consistent with that in p+p collisions. In contrast, strange particles which are extracted from the region perpendicular to reconstructed jets, i.e. underlying event, have baryon-to-meson ratio consistent with that of inclusively produced particles, both in p+p as well as p+Pb collisions. These data could be used for further tests of accuracy of strangeness production in various Monte-Carlo generators, not only PYTHIA which was chosen as an example.

Finally, we discuss the transverse momentum dependence of the Λ/K^0_S ratio associated with jet production and compare it with that for inclusive particle production in Pb+Pb collisions at $\sqrt{s_{NN}}$ = 2.76 TeV. The results for central Pb+Pb collisions are shown in Figure 3.19. In Pb+Pb collisions, where the large underlying and fluctuating background significantly impacts jet reconstruction and consequently also the selection of a hard process in the analysis, the study focused on the jet resolution parameter $R = 0.2$ and in addition also applied the p_{T} cut on the leading charged hadron in the reconstructed jet, similarly as in inclusive jet analyses described earlier. The results demonstrate that the production of strange particles associated with jet fragmentation does not, within current experimental uncertainties, depend on the minimum threshold for the jet selection. Similarly to high-multiplicity p+Pb results, the Λ/K^0_S ratio associated with hard scattering in central Pb+Pb collisions is significantly smaller than the corresponding ratio for inclusively produced particles.

In summary, the measured Λ/K^0_S ratios associated with jet production clearly show that the baryon-to-meson enhancement observed in high-multiplicity p+Pb or Pb+Pb collisions in general, does not originate from modified jet fragmentation, and other hadronization scenarios are at play, most likely connected to some extent with parton coalescence and recombination and its interplay with fragmentation. In upcoming data taking periods at the LHC, ALICE will perform more detailed studies benefiting from newer, high statistics data sets, as well as upgraded ALICE inner tracking detector to study in detail also the charm quark sector.

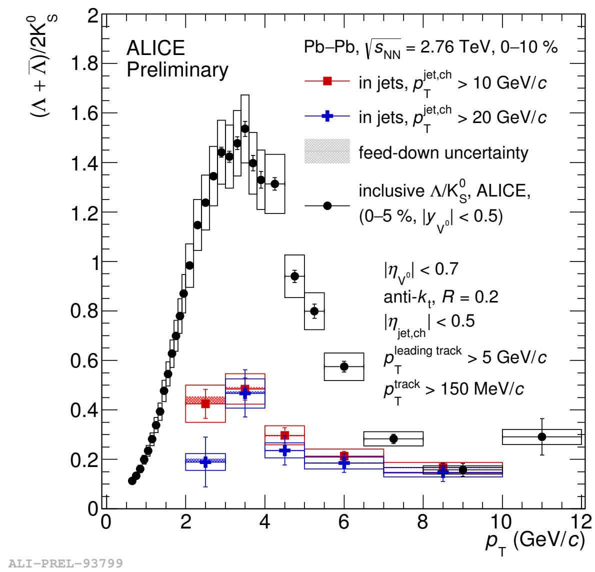

Figure 3.19: Λ/K^0_S ratio in charged-particle jets and in bulk in central Pb+Pb collisions at $\sqrt{s_{NN}}$ = 2.76 TeV. Results are shown for charged-particle jets with R = 0.2 and p_T> 10 GeV/c and p_T> 20 GeV/c, respectively.

3.7 Jet substructure measurements

Jets are rich objects and studies of their inner structure provide a multi-scale probe of QCD. Although jet substructure is of primary interest to particle physics, recently is also beeing explored in heavy-ion collisions [142, 143] to help improve understanding of hadronization mechanisms and the nature of jet quenching. Jet grooming algorithms provide access to the high-momentum transfer (hard) parton splittings inside a jet by removing soft wide-angle radiation. The commonly used Soft Drop (SD) grooming algorithm [144–146] identifies a single splitting by reclustering the constituents of a jet using the Cambridge/Aachen (C/A) algorithm [147]. The grooming procedure is graphically shown in Figure 3.20. The splitting is selected from within the history of the reclustering with a grooming condition, $z > z_\mathrm{cut}\theta^\beta$. β and z_cut are free parameters, z corresponds the fraction of transverse momentum carried by the sub-leading (lowest p_T) prong,

$$z \equiv \frac{p_\mathrm{T,sublead}}{p_\mathrm{T,lead} + p_\mathrm{T,sublead}}, \tag{3.5}$$

and θ is the relative angular distance between the leading and sub-leading prong,

$$\theta \equiv \frac{\sqrt{\Delta y^2 + \Delta\varphi^2}}{R}. \tag{3.6}$$

In the latter equation, Δy and $\Delta\varphi$ are the distances measured in rapidity and azimuthal angle, respectively, and R is the jet resolution parameter (radius). The groomed splitting is then commonly characterized by the groomed momentum fraction, z_g, and the (scaled) groomed jet radius, θ_g, which are the values of z and θ of Eq. (3.6) and (3.5) for the identified splitting.

The ALICE collaboration has recently published measurements of the θ_g and z_g distributions in Pb+Pb collisions at $\sqrt{s_{NN}}$ = 5.02 TeV [148] which are presented in Figure 3.21.

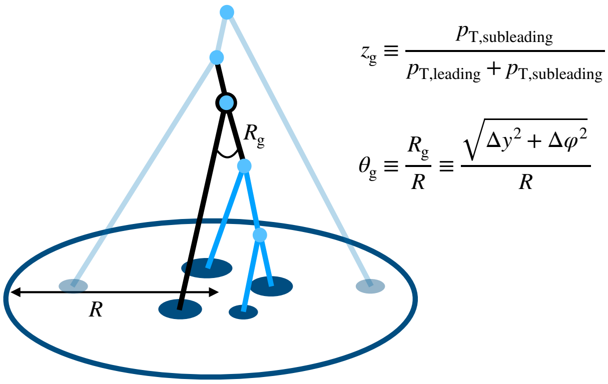

Figure 3.20: Scheme of the angularly ordered Cambridge-Aachen reclustering of jet constituents and subsequent Soft Drop grooming procedure [144]. The identified splitting is denoted in black and the splittings that were groomed away in light blue. Figure taken from [148].

While no significant modification of the z_g distribution in central Pb+Pb collisions compared to p+p collisions is observed, a narrowing of the θ_g distribution compared to p+p collisions is seen. This is the first direct evidence of the modification of the angular structure of jets in the QGP. The observed θ_g narrowing is consistent with models based on medium-modified quark/gluon fractions with coherent energy loss as well as calculations based on incoherent interaction of the jet constituents with the medium. Further studies are therefoe needed to discriminate between the mechanisms.

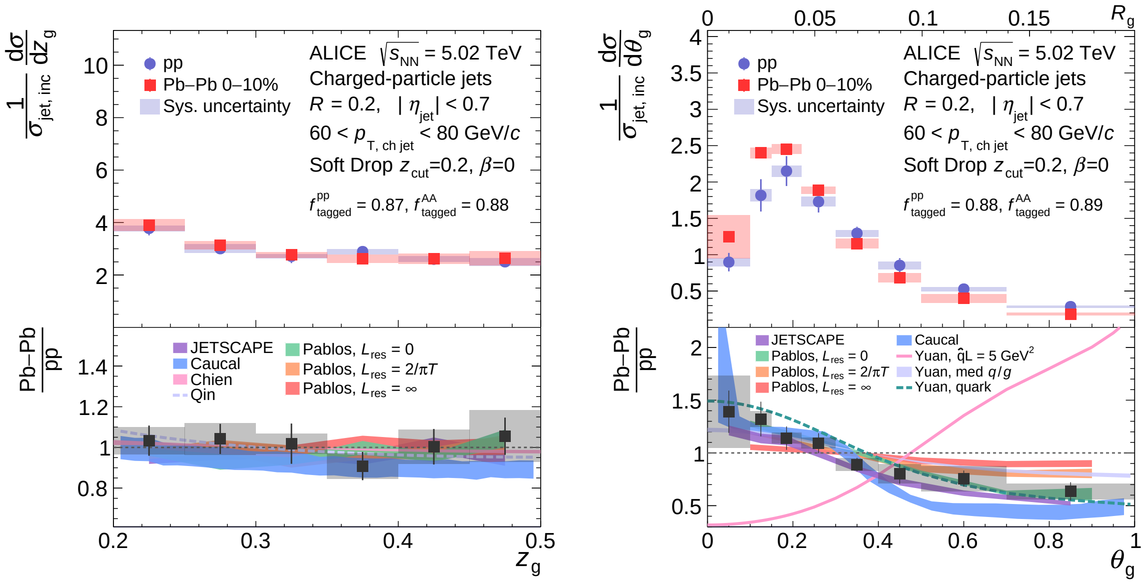

Figure 3.21: z_g (left) and θ_g (right) distributions for charged-particle jets in central Pb+Pb collisions at $\sqrt{s_{NN}}$ = 5.02 TeV compared to p+p data with z_{cut} = 0.2 and R = 0.2. The ratios in the bottom panel show models comparisons: JETSCAPE [124], Caucal [149, 150], Chien [151], Qin [152], Pablos [74, 123, 153], and Yuan [154].

Chapter 4

Summary and outlook

Heavy-ion collisions are a unique and rich laboratory that enables to study, with some control by using different collision systems and collision energies, various aspects of QCD. Understanding of properties of the quark-gluon plasma created in energetic collisions of heavy ions at RHIC and LHC energies requires, however, well calibrated probes. Jets, to which this lecture was devoted, arise from initial hard parton scattering and provide one of the tools with great potential for the QGP tomography. While travelling through the hot and dense medium, jets are expected to be influenced by the structure of the medium at many length scales. However, measuring these in-medium modifications of jets and extracting information about the structure of the QGP present many challenges, both on experimental and theoretical side, as I have presented.

The lessons learned so far starting from jet quenching observed in inclusive particle spectra at high transverse momentum, followed by di-hadron correlations up to fully reconstructed jets are very promising. These studies have shown that the interaction of a jet with the medium does not alter the direction of the jet as a whole and that while the energy loss is substantial, the depleted jets emerging from the QGP medium are essentialy unmodified. The data also show that the energy lost manifests in increased production of many low-momentum particles that are spread over large angles away from the jet direction. The first direct experimental evidence for the modification of the angular scale of groomed jets in heavy-ion collisions at the LHC energy demonstrates sensitivity to the microscopic structure of the QGP, including its angular resolving power. This marks a crucial step towards quantitative understanding of the properties of the QGP using novel differential jet substructure measurements.

The advances in jet observables studied will benefit also from new high statistics data and upgrades of major experiments at RHIC and the LHC, which will enable to fullfil the promise of jets as QGP microscopes. The Au+Au data to be measured at RHIC in 2023 and 2025 along with the Run 3 and Run 4 measurements in Pb+Pb collisions at the LHC will bring another significant increase in sampled integrated luminosity. These new data sets will enable to perform microscopic tomographic studies of the QGP with improved detectors, including a new sPHENIX experiment currently being assembled at BNL. In 2024, the STAR and sPHENIX experiments will also collect high statistics p+p and p+Au datasets to perform studies of fundamental QCD and cold nuclear matter effects including the forward rapidity region. This will offer the unique possibility to search for saturation physics in the incoming gold nucleus and prepare the research community at RHIC for the transition to the new Electron Ion Collider which is expected to become operational early 2030's.

Bibliography

[1] J. C. Collins and M. J. Perry *Phys. Rev. Lett.* **34** (1975) 1353.

[2] E. V. Shuryak *Phys. Rept.* **61** (1980) 71–158.

[3] F. Karsch *Nucl. Phys. A* **698** (2002) 199–208.

[4] Y. Aoki, G. Endrodi, Z. Fodor, S. D. Katz, and K. K. Szabo *Nature* **443** (2006) 675–678.

[5] D. Thomas, D. N. Schramm, K. A. Olive, G. J. Mathews, B. S. Meyer, and B. D. Fields *Astrophys. J.* **430** (1994) 291–299.

[6] STAR. `https://drupal.star.bnl.gov/STAR/files/BES_WPII_ver6.9_Cover.pdf`.

[7] **STAR** Collaboration, L. Adamczyk *et al. Phys. Rev. C* **96** no. 4, (2017) 044904.

[8] A. Andronic, P. Braun-Munzinger, K. Redlich, and J. Stachel *Nature* **561** no. 7723, (2018) 321–330.

[9] Z. Citron *et al. CERN Yellow Rep. Monogr.* **7** (2019) 1159–1410.

[10] A. Andronic, P. Braun-Munzinger, and J. Stachel *Nucl. Phys. A* **834** (2010) 237C–240C.

[11] J. Cleymans, H. Oeschler, K. Redlich, and S. Wheaton *Phys. Rev. C* **73** (2006) 034905.

[12] A. Bazavov *et al. Phys. Rev. D* **85** (2012) 054503.

[13] O. Kaczmarek, F. Karsch, E. Laermann, C. Miao, S. Mukherjee, P. Petreczky, C. Schmidt, W. Soeldner, and W. Unger *Phys. Rev. D* **83** (2011) 014504.

[14] A. Bzdak, S. Esumi, V. Koch, J. Liao, M. Stephanov, and N. Xu *Phys. Rept.* **853** (2020) 1–87.

[15] M. A. Stephanov, K. Rajagopal, and E. V. Shuryak *Phys. Rev. Lett.* **81** (1998) 4816–4819.

[16] M. A. Stephanov *Prog. Theor. Phys. Suppl.* **153** (2004) 139–156.

[17] Z. Fodor and S. D. Katz *JHEP* **04** (2004) 050.

[18] S. Datta, R. V. Gavai, and S. Gupta *Nucl. Phys. A* **904-905** (2013) 883c–886c.

[19] Y.-J. Lee, A. S. Yoon, and W. Busza.
`http://web.mit.edu/mithig/movies/LHCanmation.mov`.

[20] J. D. Bjorken *Phys. Rev. D* **27** (1983) 140–151.

[21] **PHENIX** Collaboration, S. S. Adler *et al. Phys. Rev. C* **71** (2005) 034908. [Erratum: Phys.Rev.C 71, 049901 (2005)].

[22] P. Huovinen and P. Petreczky *Nucl. Phys. A* **837** (2010) 26–53.

[23] U. Heinz and R. Snellings *Ann. Rev. Nucl. Part. Sci.* **63** (2013) 123–151.

[24] P. Romatschke and U. Romatschke, *Relativistic Fluid Dynamics In and Out of Equilibrium.* Cambridge Monographs on Mathematical Physics. Cambridge University Press, 5, 2019.

[25] J.-Y. Ollitrault *Phys. Rev. D* **46** (1992) 229–245.

[26] S. Voloshin and Y. Zhang *Z. Phys. C* **70** (1996) 665–672.

[27] A. M. Poskanzer and S. A. Voloshin *Phys. Rev. C* **58** (1998) 1671–1678.

[28] **STAR** Collaboration, J. Adams *et al. Phys. Rev. Lett.* **92** (2004) 052302.

[29] **STAR** Collaboration, J. Adams *et al. Phys. Rev. Lett.* **95** (2005) 122301.

[30] **PHENIX** Collaboration, A. Adare *et al. Phys. Rev. Lett.* **98** (2007) 162301.

[31] P. Kovtun, D. T. Son, and A. O. Starinets *Phys. Rev. Lett.* **94** (2005) 111601.

[32] **STAR** Collaboration, M. Abdallah *et al.* `arXiv:2108.00908 [nucl-ex]`.

[33] D. Molnar and S. A. Voloshin *Phys. Rev. Lett.* **91** (2003) 092301.

[34] R. J. Fries, B. Muller, C. Nonaka, and S. A. Bass *Phys. Rev. C* **68** (2003) 044902.

[35] V. Greco, C. M. Ko, and P. Levai *Phys. Rev. C* **68** (2003) 034904.

[36] **PHENIX** Collaboration, A. Adare *et al. Phys. Rev. C* **85** (2012) 064914.

[37] **ALICE** Collaboration, B. Abelev *et al. JHEP* **06** (2015) 190.

[38] **ALICE** Collaboration, J. Adam *et al. JHEP* **09** (2016) 164.

[39] **ALICE** Collaboration, S. Acharya *et al. JHEP* **09** (2018) 006.

[40] **STAR** Collaboration, G. Agakishiev *et al. Phys. Rev. Lett.* **108** (2012) 072301.

[41] H. Song and U. W. Heinz *Phys. Lett. B* **658** (2008) 279–283.

[42] H. Song and U. W. Heinz *Phys. Rev. C* **77** (2008) 064901.

[43] H. Song and U. W. Heinz *Phys. Rev. C* **78** (2008) 024902.

[44] H. Song, S. A. Bass, and U. Heinz *Phys. Rev. C* **83** (2011) 054912. [Erratum: Phys.Rev.C 87, 019902 (2013)].

[45] K. Werner *Phys. Rev. Lett.* **109** (2012) 102301.

[46] **ALICE** Collaboration, B. Abelev *et al. Phys. Rev. Lett.* **111** (2013) 222301.

[47] **STAR** Collaboration, B. I. Abelev *et al. Phys. Rev. Lett.* **97** (2006) 152301.

[48] **STAR** Collaboration, B. I. Abelev *et al. Phys. Lett. B* **655** (2007) 104–113.

[49] **STAR** Collaboration, J. Adam *et al. Phys. Rev. Lett.* **124** no. 17, (2020) 172301.

[50] **ALICE** Collaboration, S. Acharya *et al. Phys. Lett. B* **793** (2019) 212–223.

[51] R. J. Fries, B. Muller, C. Nonaka, and S. A. Bass *Phys. Rev. Lett.* **90** (2003) 202303.

[52] V. Greco, C. M. Ko, and P. Levai *Phys. Rev. Lett.* **90** (2003) 202302.

[53] R. C. Hwa and C. B. Yang *Phys. Rev. C* **67** (2003) 034902.

[54] R. C. Hwa and C. B. Yang *Phys. Rev. C* **70** (2004) 024905.

[55] M. Gyulassy and X.-N. Wang *Nucl. Phys. B* **420** (1994) 583–614.

[56] X.-N. Wang, M. Gyulassy, and M. Plumer *Phys. Rev. D* **51** (1995) 3436–3446.

[57] R. Baier, Y. L. Dokshitzer, S. Peigne, and D. Schiff *Phys. Lett. B* **345** (1995) 277–286.

[58] R. Baier, Y. L. Dokshitzer, A. H. Mueller, S. Peigne, and D. Schiff *Nucl. Phys. B* **483** (1997) 291–320.

[59] R. Baier, Y. L. Dokshitzer, A. H. Mueller, S. Peigne, and D. Schiff *Nucl. Phys. B* **484** (1997) 265–282.

[60] R. Baier, Y. L. Dokshitzer, A. H. Mueller, and D. Schiff *Nucl. Phys. B* **531** (1998) 403–425.

[61] B. G. Zakharov *JETP Lett.* **63** (1996) 952–957.

[62] B. G. Zakharov *JETP Lett.* **65** (1997) 615–620.

[63] A. Majumder and M. Van Leeuwen *Prog. Part. Nucl. Phys.* **66** (2011) 41–92.

[64] N. Armesto *et al. Phys. Rev. C* **86** (2012) 064904.

[65] Y. Mehtar-Tani, J. G. Milhano, and K. Tywoniuk *Int. J. Mod. Phys. A* **28** (2013) 1340013.

[66] J.-P. Blaizot and Y. Mehtar-Tani *Int. J. Mod. Phys. E* **24** no. 11, (2015) 1530012.

[67] **STAR** Collaboration, J. Adams *et al. Phys. Rev. Lett.* **91** (2003) 172302.

[68] **STAR** Collaboration, J. Adams *et al. Phys. Rev. Lett.* **91** (2003) 072304.

[69] **STAR** Collaboration, C. Adler *et al. Phys. Rev. Lett.* **89** (2002) 202301.

[70] **PHENIX** Collaboration, K. Adcox *et al. Phys. Rev. Lett.* **88** (2002) 022301.

[71] **PHOBOS** Collaboration, B. B. Back *et al. Phys. Lett. B* **578** (2004) 297–303.

[72] M. L. Miller, K. Reygers, S. J. Sanders, and P. Steinberg *Ann. Rev. Nucl. Part. Sci.* **57** (2007) 205–243.

[73] Y.-T. Chien, A. Emerman, Z.-B. Kang, G. Ovanesyan, and I. Vitev *Phys. Rev. D* **93** no. 7, (2016) 074030.

[74] J. Casalderrey-Solana, D. C. Gulhan, J. G. Milhano, D. Pablos, and K. Rajagopal *JHEP* **10** (2014) 019. [Erratum: JHEP 09, 175 (2015)].

[75] J. Xu, J. Liao, and M. Gyulassy *JHEP* **02** (2016) 169.

[76] C. Andrés, N. Armesto, M. Luzum, C. A. Salgado, and P. Zurita *Eur. Phys. J. C* **76** no. 9, (2016) 475.

[77] E. Bianchi, J. Elledge, A. Kumar, A. Majumder, G.-Y. Qin, and C. Shen `arXiv:1702.00481 [nucl-th]`.

[78] **CMS** Collaboration, V. Khachatryan *et al. JHEP* **04** (2017) 039.

[79] K. J. Eskola and H. Honkanen *Nucl. Phys. A* **713** (2003) 167–187.

[80] S. R. Klein and R. Vogt *Phys. Rev. Lett.* **91** (2003) 142301.

[81] **PHENIX** Collaboration, A. Adare *et al. Phys. Rev. C* **87** no. 3, (2013) 034911.

[82] **CMS** Collaboration, S. Chatrchyan *et al. Eur. Phys. J. C* **72** (2012) 1945.

[83] **ALICE** Collaboration, E. Abbas *et al. Phys. Lett. B* **726** (2013) 610–622.

[84] **ATLAS** Collaboration, G. Aad *et al. JHEP* **09** (2015) 050.

[85] **STAR** Collaboration, C. Adler *et al. Phys. Rev. Lett.* **90** (2003) 082302.

[86] **STAR** Collaboration, J. Adams *et al. Phys. Rev. Lett.* **97** (2006) 162301.

[87] **STAR** Collaboration, C. Adler *et al. Phys. Rev. Lett.* **90** (2003) 032301.

[88] B. Muller *Phys. Rev. C* **67** (2003) 061901.

[89] A. Drees, H. Feng, and J. Jia *Phys. Rev. C* **71** (2005) 034909.

[90] A. Dainese, C. Loizides, and G. Paic *Eur. Phys. J. C* **38** (2005) 461–474.

[91] K. J. Eskola, H. Honkanen, C. A. Salgado, and U. A. Wiedemann *Nucl. Phys. A* **747** (2005) 511–529.

[92] T. Renk *Phys. Rev. C* **88** no. 5, (2013) 054902.

[93] **STAR** Collaboration, S. Salur *Eur. Phys. J. C* **61** (2009) 761–767.

[94] **STAR** Collaboration, M. Ploskon *Nucl. Phys. A* **830** (2009) 255C–258C.

[95] **STAR** Collaboration, J. Adam *et al. Phys. Rev. C* **102** no. 5, (2020) 054913.

[96] **ALICE** Collaboration, B. Abelev *et al. JHEP* **03** (2012) 053.

[97] **ALICE** Collaboration, H. Bossi *PoS* **HardProbes2020** (2021) 135.

[98] **ATLAS** Collaboration, G. Aad *et al. Phys. Rev. Lett.* **105** (2010) 252303.

[99] **CMS** Collaboration, S. Chatrchyan *et al. Phys. Rev. C* **84** (2011) 024906.

[100] **ALICE** Collaboration, B. Abelev *et al. JHEP* **03** (2014) 013.

[101] T. Sjostrand, S. Mrenna, and P. Z. Skands *JHEP* **05** (2006) 026.

[102] P. Z. Skands *Phys. Rev. D* **82** (2010) 074018.

[103] **PHENIX** Collaboration, S. S. Adler *et al. Phys. Rev. C* **69** (2004) 034910.

[104] I. Vitev and B.-W. Zhang *Phys. Rev. Lett.* **104** (2010) 132001.

[105] Y.-T. Chien and I. Vitev *JHEP* **05** (2016) 023.

[106] J. Casalderrey-Solana, D. Gulhan, G. Milhano, D. Pablos, and K. Rajagopal *JHEP* **03** (2017) 135.

[107] W. Ke, Y. Xu, and S. A. Bass *Phys. Rev. C* **100** no. 6, (2019) 064911.

[108] **ALICE** Collaboration, S. Acharya *et al. Phys. Rev. C* **101** no. 3, (2020) 034911.

[109] **ATLAS** Collaboration, G. Aad *et al. Phys. Lett. B* **719** (2013) 220–241.

[110] **ATLAS** Collaboration *ATLAS-CONF-2019-056* .

[111] **CMS** Collaboration *CMS-PAS-HIN-18-014* .

[112] K. C. Zapp, F. Krauss, and U. A. Wiedemann *JHEP* **03** (2013) 080.

[113] R. Kunnawalkam Elayavalli and K. C. Zapp *Eur. Phys. J. C* **76** no. 12, (2016) 695.

[114] I. Vitev and B.-W. Zhang *Phys. Lett. B* **669** (2008) 337–344.

[115] R. Sharma, I. Vitev, and B.-W. Zhang *Phys. Rev. C* **80** (2009) 054902.

[116] Y. He, S. Cao, W. Chen, T. Luo, L.-G. Pang, and X.-N. Wang *Phys. Rev. C* **99** no. 5, (2019) 054911.

[117] Y. He, T. Luo, X.-N. Wang, and Y. Zhu *Phys. Rev. C* **91** (2015) 054908. [Erratum: Phys.Rev.C 97, 019902 (2018)].

[118] Z.-B. Kang, F. Ringer, and I. Vitev *Phys. Lett. B* **769** (2017) 242–248.

[119] A. Idilbi and A. Majumder *Phys. Rev. D* **80** (2009) 054022.

[120] D. Butter and S. M. Kuzenko *JHEP* **11** (2011) 080.

[121] H. T. Li and I. Vitev *Phys. Lett. B* **793** (2019) 259–264.

[122] J. Casalderrey-Solana, D. C. Gulhan, J. G. Milhano, D. Pablos, and K. Rajagopal *JHEP* **03** (2016) 053.

[123] Z. Hulcher, D. Pablos, and K. Rajagopal *JHEP* **03** (2018) 010.

[124] J. H. Putschke *et al.* `arXiv:1903.07706 [nucl-th]`.

[125] X.-N. Wang and Y. Zhu *Phys. Rev. Lett.* **111** no. 6, (2013) 062301.

[126] F. D'Eramo, M. Lekaveckas, H. Liu, and K. Rajagopal *JHEP* **05** (2013) 031.

[127] **ALICE** Collaboration, J. Adam *et al. JHEP* **09** (2015) 170.

[128] **STAR** Collaboration, L. Adamczyk *et al. Phys. Rev. C* **96** no. 2, (2017) 024905.

[129] **ALICE** Collaboration, J. Norman *PoS* **HardProbes2020** (2021) 127.

[130] **ALICE** Collaboration, B. Abelev *et al. Phys. Lett. B* **722** (2013) 262–272.

[131] **CMS** Collaboration, S. Chatrchyan *et al. Phys. Rev. D* **90** no. 7, (2014) 072006.

[132] G. Soyez *Phys. Lett. B* **698** (2011) 59–62.

[133] M. Dasgupta, F. A. Dreyer, G. P. Salam, and G. Soyez *JHEP* **06** (2016) 057.

[134] **ALICE** Collaboration, B. B. Abelev *et al. Phys. Rev. D* **91** no. 11, (2015) 112012.

[135] D. de Florian *Phys. Rev. D* **79** (2009) 114014.

[136] M. Bahr *et al. Eur. Phys. J. C* **58** (2008) 639–707.

[137] **STAR** Collaboration, L. Adamczyk *et al. Phys. Rev. Lett.* **119** no. 6, (2017) 062301.

[138] **JETSCAPE** Collaboration, K. Kauder *et al. Nucl. Phys. A* **982** (2019) 615–618.

[139] **CMS** Collaboration, V. Khachatryan *et al. JHEP* **11** (2016) 055.

[140] **STAR** Collaboration, N. R. Sahoo *PoS* **HardProbes2020** (2021) 132.

[141] **ALICE** Collaboration, S. Acharya *et al.* `arXiv:2105.04890 [nucl-ex]`.

[142] **CMS** Collaboration, A. M. Sirunyan *et al. Phys. Rev. Lett.* **120** no. 14, (2018) 142302.

[143] **ALICE** Collaboration, S. Acharya *et al. Phys. Lett. B* **802** (2020) 135227.

[144] A. J. Larkoski, S. Marzani, G. Soyez, and J. Thaler *JHEP* **05** (2014) 146.

[145] M. Dasgupta, A. Fregoso, S. Marzani, and G. P. Salam *JHEP* **09** (2013) 029.

[146] A. J. Larkoski, S. Marzani, and J. Thaler *Phys. Rev. D* **91** no. 11, (2015) 111501.

[147] Y. L. Dokshitzer, G. D. Leder, S. Moretti, and B. R. Webber *JHEP* **08** (1997) 001.

[148] **ALICE** Collaboration, S. Acharya *et al.* `arXiv:2107.12984 [nucl-ex]`.

[149] P. Caucal, E. Iancu, and G. Soyez *JHEP* **10** (2019) 273.

[150] P. Caucal, E. Iancu, A. H. Mueller, and G. Soyez *Phys. Rev. Lett.* **120** (2018) 232001, `arXiv:1801.09703 [hep-ph]`.

[151] Y.-T. Chien and I. Vitev *Phys. Rev. Lett.* **119** no. 11, (2017) 112301.

[152] N.-B. Chang *PoS* **HardProbes2018** (2019) 076.

[153] J. Casalderrey-Solana, G. Milhano, D. Pablos, and K. Rajagopal *JHEP* **01** (2020) 044.

[154] F. Ringer, B.-W. Xiao, and F. Yuan *Phys. Lett. B* **808** (2020) 135634.